Check for updates

Received: 18 February 2023 | Accepted: 8 September 2023

DOI: 10.1111/1365-2478.13425

Geophysical Prospecting | EAGE EUROPEAN ASSOCIATION OF GEOSCIENTISTS & ENGINEERS

ORIGINAL ARTICLE

# Well-log integration and seismic-to-well tie off George V Land (Antarctica)

**Davide Gei** | **Giuliano Brancolini** | **Laura De Santis** | **Riccardo Geletti**

Istituto Nazionale di Oceanografia e di Geofisica Sperimentale (OGS), Sgonico, Trieste, Italy

**Correspondence**
Davide Gei, Istituto Nazionale di Oceanografia e di Geofisica Sperimentale (OGS), Borgo Grotta Gigante 42c, 34010 Sgonico, Trieste, Italy. Email: dgei@ogs.it

**Abstract**

Cenozoic sediments from the continental rise off the George V Land consist of silty/clayey facies variably rich in diatom ooze; these sediments hold a record of the glacial history of the Wilkes Subglacial Basin and are important for estimating the contribution of the East Antarctic Ice Sheet to global sea level changes during past transition to warmer climates. This is fundamental to predict future scenarios related to the global warming. The petrophysical properties of Antarctic marine sediments are influenced by the ice sheet dynamics and may affect the amplitude of seismic reflections. Through a seismic-to-well tie procedure, we investigate the origin of high amplitude reflections from Miocene-early Pliocene deposits identified in two seismic lines crossing at the Integrated Ocean Drilling Program Expedition 318 drill site U1359. Downhole and core log measurements are preconditioned and merged to obtain complete velocity and density records from the sea floor to the bottom of the deepest of the four wells drilled at this site. We generate a synthetic trace by convolving the reflectivity series with the seismic wavelet obtained from the sea-floor reflection and match the synthetic trace to the seismic data with a time variant cross-correlation procedure. This procedure established a robust time-depth relationship, not achievable from the available small-offset seismic data. To our knowledge, this is the first seismic-to-well tying in the George V Land area. Based on results from synthetic data, the anomalous high amplitude seismic package can be linked to changes in density of sediments. Such changes are interpreted as representative for the alternation of diatom-rich (warm climate) and silty-clay layers with ice-rafted debris (cold climate) inside the deposits. We suggest that the analysis of the characteristics and the distribution of similar seismic anomaly around Antarctica can give insight into the modality of past Antarctic ice sheet dynamics.

**KEYWORDS**

borehole geophysics, data processing, logging, modelling, seismics

## INTRODUCTION

One component of the pelagic sediment around Antarctica is the diatom ooze that mostly occurs between the northern extent of the Antarctic Polar Front Zone and the northern limit of the summer sea ice (Dutkiewicz et al., 2016). Another sedimentary facies peculiar of Antarctic margins is diamicton, made of silty/clay with ice-rafted debris of variable size, typically originated by subglacial erosion and ice proximal to distal deposition on continental margin, during ice sheet

This is an open access article under the terms of the Creative Commons Attribution-NonCommercial License, which permits use, distribution and reproduction in any medium, provided the original work is properly cited and is not used for commercial purposes.
© 2023 The Authors. *Geophysical Prospecting* published by John Wiley & Sons Ltd on behalf of European Association of Geoscientists & Engineers.

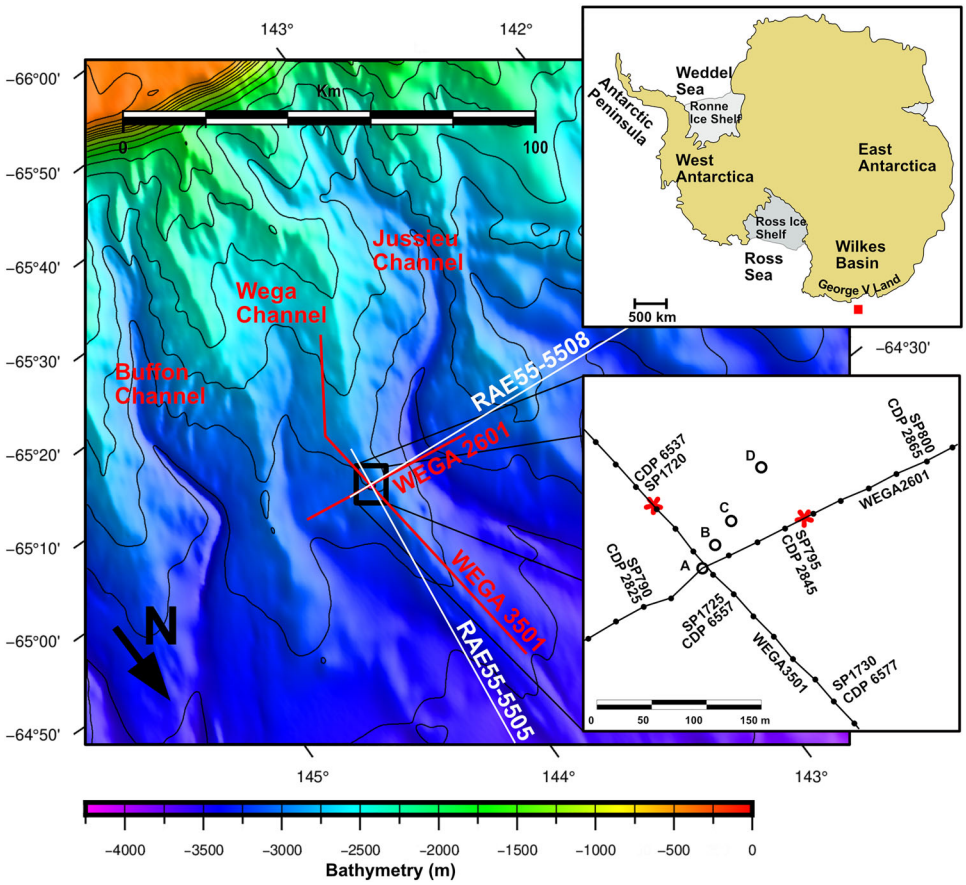


**FIGURE 1** Bathymetric map showing the study area (from IBCSOv2 of Dorschel et al., 2022) and location of the Italian-Australian WilkEs basin GlAcial history (WEGA) and the 55th Russian Antarctic Expedition (RAE) seismic lines. The isobath contour interval is 250 m. The red square in the upper right inset shows the location of the study area with respect to the Antarctic Continent. The lower right inset shows a detail of the Site U1359 with wells A, B, C, D and the WEGA lines considered in this study; the numbers along the seismic lines indicate shot points (SP) and common depth points (CDP), and the red stars indicate the position of the best-fit field-synthetic traces.

advance and retreat, and icebergs calving. The presence in the sediments of diamicton and diatom ooze is related to cold and warm climate conditions, respectively. For these reasons, the amount and distribution of these sedimentary facies are considered important palaeo-environmental indicators (e.g. Tauxe et al., 2012).

The George V Land lies at the continental margin of the East Antarctica (Figure 1). Sediments recovered from this area hold a record of the glacial history of the Wilkes Subglacial Basin (WSB), a 400 km-long and ca. 200–600 km-wide tectonic depression (Ferraccioli et al., 2009). WSB is deeply eroded by the ice sheet and the sediments from its continental margin document ice sheet significant retreat, occurred during Quaternary and late Cenozoic interglacials (Blackburn et al., 2020; Cook et al., 2013; Iizuka et al., 2023; Orejola & Passchier, 2014; Wilson et al., 2018). The study of the George V Land sediments composition (diamicton vs. diatom-rich) is therefore crucial for estimating the contribution of the marine-based East Antarctic Ice Sheet to global sea level changes during past transition to warmest climates (Escutia et al., 2011), which is fundamental to predict future scenarios related to global warming.

The study area is characterized by the presence of several N–S-trending channels and sedimentary ridges, which run perpendicular to the margin (Figure 1); these features were formed by turbidity flows and hemipelagic drape deposits, influenced and reworked by bottom currents. Site U1359 was drilled in 2010 on the eastern levee of the Jussieu Channel, as part of the Integrated Ocean Drilling Program (IODP) Expedition 318 (Escutia et al., 2011). This site was selected to study the sedimentary sequence from the late Miocene to Present (Escutia et al., 2011). This period is of particular relevance because it includes the transition from temperate, generally warmer, to polar, colder conditions on most of the Antarctic continent.

In the framework of the Italian-Australian WilkEs basin GlAcial history (WEGA) project, a geological–geophysical survey was conducted along the George V and Wilkes Land continental rise in January–March 2000. The aim of the project was to reconstruct the late Cenozoic evolution of this

13652478, 0, Downloaded from https://onlinelibrary.wiley.com/doi/10.1111/1365-2478.13425 by Ogs Trieste Istituto Nazionale, Wiley Online Library on [13/11/2023]. See the Terms and Conditions (https://onlinelibrary.wiley.com/terms-and-conditions) on Wiley Online Library for rules of use; OA articles are governed by the applicable Creative Commons License

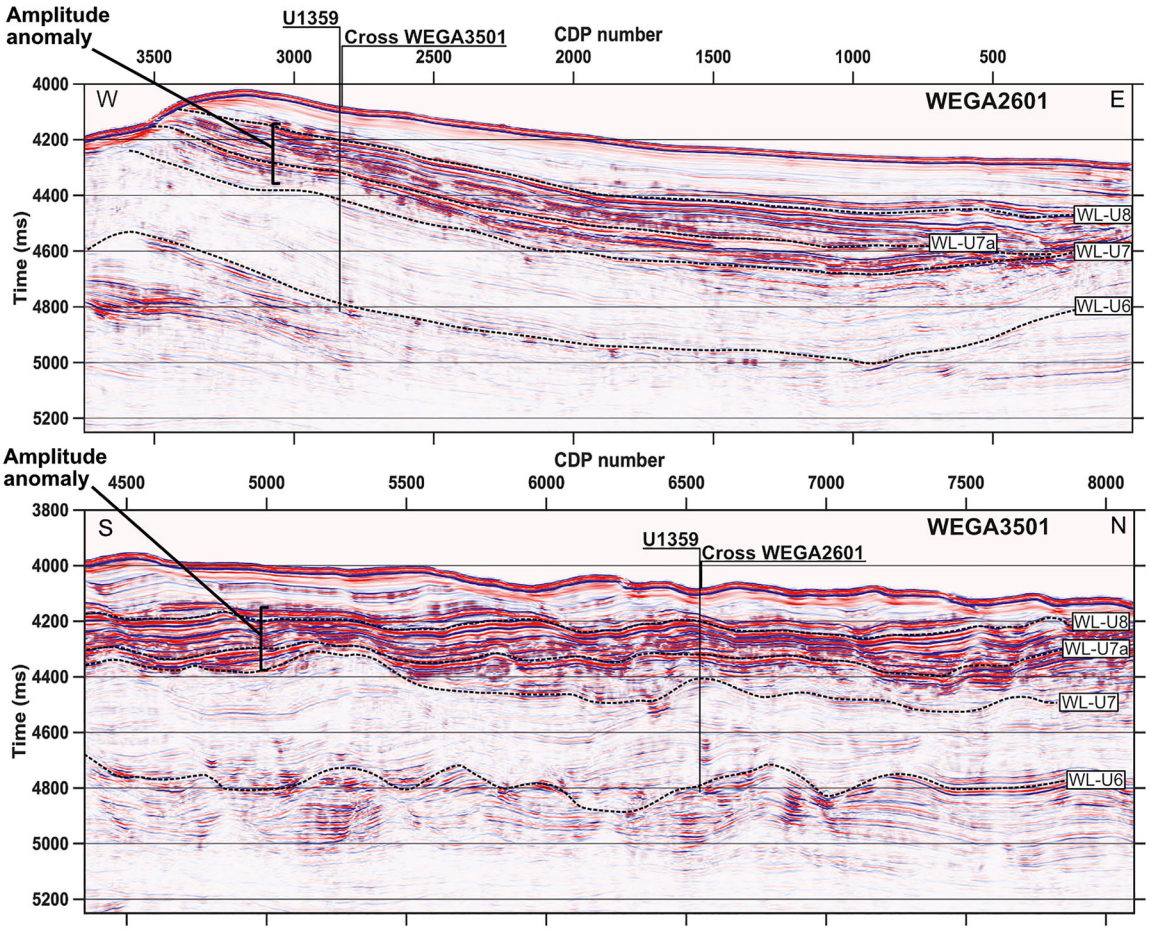


**FIGURE 2** Time migrated seismic sections WEGA2601 and WEGA3501 with the positions of the cross-point and of the drilling site U1359. The main unconformities are indicated by the black-dashed lines, and the reflection package characterized by high seismic amplitude is clearly marked.

part of the East Antarctic margin and the survey included the acquisition of 1827 km of high-resolution multi-channel seismic reflection data. Figure 1 shows the location of two WEGA profiles crossing at site U1359. The WEGA seismic data acquired along the eastern levee of the Jussieu Channel show a reflection package between unconformities WL-U7 and WL-U8 characterized by a strong amplitude anomaly (Figure 2). The presence of widespread seismic amplitude anomalies in deep water sediment depends on the petrophysical properties of the sedimentary sequence which, in turn, are influenced by changes in bottom currents regime, turbidity flows or, more generally, sediment supply. This latter is normally produced by tectonic or eustatic events. In Antarctica, further processes must be considered: the settlement, dynamics and regime of the Antarctic ice sheet. Deciphering the origin of the seismic amplitude anomalies from the Antarctic data is a tool for constraining entity and distribution of geological processes possibly related to the Earth climate, and relevant at global scale.

To understand the origin of the seismic amplitude anomaly, we estimate the physical properties of the sediments from downhole and core log measurements at site U1359 and obtain a synthetic trace to correlate with two WEGA seismic sections in proximity of the drill site. The synthetic trace is computed from the reflectivity series using the density and sonic logs and time to depth relationships (White & Simm, 2003). Moreover, this procedure is a valuable option for estimating the depth of the main geological structures when velocity information cannot be inferred from the seismic data, for example short-offset datasets. This approach can also be applied in other situations, such as busy harbour areas, narrow fjords or sea ice-covered waters, where the acquisition of multi-channel seismic profiles with a long streamer is not possible, and only single-channel or short-streamer reflection seismic data can be acquired.

Mis-ties between experimental and synthetic data can be corrected by stretching and squeezing the synthetic trace, traditionally performed manually, but recently executed with automatic procedures; we consider the time variant cross-correlation (Cho, 2013; Cui & Margrave, 2015; Hale, 2009). The application of time-shift corrections to the synthetic trace results in alterations of the measured P-wave velocities; we

13652478, 0, Downloaded from https://onlinelibrary.wiley.com/doi/10.1111/1365-2478.13425 by Ogs Trieste Istituto Nazionale, Wiley Online Library on [13/11/2023]. See the Terms and Conditions (https://onlinelibrary.wiley.com/terms-and-conditions) on Wiley Online Library for rules of use; OA articles are governed by the applicable Creative Commons License

**TABLE 1** Seismic acquisition parameters of the WEGA seismic lines.

| | | | |
|---|---|---|---|
| Source | 2 GI-Gun 6.8 L | Streamer length | 500 m |
| Source depth | 3 m | Streamer depth | 10 m |
| Shot interval | 25 m | Number of traces/shot | 40 |
| Fold | 10 | Group interval | 12.5 m |
| Time sampling interval | 1 ms | Min offset | 170 m |
| | | Max offset | 657.5 m |

compute the modified velocity profile and verify the absence of unphysical velocity variations.

To our knowledge, this is the first attempt of seismic-to-well among the seven sites drilled in the George V Land area during the IODP Expedition 318. The procedure proposed in this study could be of interest for other IODP wells, characterized by logs data discontinuity and/or paucity.

We first describe the processing sequence applied to the seismic lines. Then, we describe the processing applied to both the downhole and the core logs of site U1359 and the integration of these two datasets. We introduce the seismic-to-well tie procedure and the comparison of the synthetic trace with seismic data, considering also an automatic technique for improving the goodness-of-fit. Finally, we produced a refinement of the seismic unconformities depth and age and propose and discuss a hypothesis about the origin of the seismic amplitude anomalies.

## PROCESSING OF LEGACY SEISMIC DATA

In this study, we consider the seismic lines WEGA2601 and WEGA3501 acquired in February–March 2000 by the vessel RV Tangaroa. The target of the seismic survey was to investigate setting and characteristics of the complex depositional environment off the George V Land, characterized by the presence of prominent channel levee systems (Brancolini & Harris, 2000). The Integrated Ocean Drilling Program site U1359 is located approximately at the seismic lines cross point. The map in Figure 1 shows the position the seismic lines with respect to the well site.

The seismic data acquisition parameters of the WEGA campaign are summarized in Table 1. The length of the streamer (500 m) is short with respect to the depth of the targets (around 3000 m below sea level). Consequently, velocity information is difficult to infer from seismic processing and may not be reliable (Yilmaz, 2001). This aspect underlines the importance of using log data for a reliable depth–time conversion, necessary for a correct reconstruction of the geological model of the area.

We reprocessed the legacy datasets with the following processing sequence: time resampling from 1 to 2 ms, data editing, bandpass filtering (3/7–140/150 Hz), spherical divergence correction, common mid-point (CMP) sorting, velocity analysis, normal move out correction, CMP stacking and frequency-wavenumber time migration. The velocity analysis is performed on the main reflectors with the semblance and common velocity stack methods. This is a manual procedure, performed by the operator and because of the small maximum offset of the WEGA seismic lines, a relatively wide range of velocities corrects the normal move out and flattens the hyperbolic reflections in common depth point (CDP) gathers. However, we verified the stack velocity profiles in proximity of site U1359 by comparison with those of two multi-channel seismic profiles from the 55th Russian Antarctic Expedition (RAE) (https://sdls.ogs.trieste.it) acquired in 2010 in the same area (Figure 1) with a longer streamer (4387.5 m) (German Leitchenkov, personal communication).

The WEGA raw data are affected by incoherent noise in the same frequency band of the primary reflections, possibly due to malfunctioning of the electronics of the streamer. With the aim of avoiding any possible signal distortion, we did not apply denoising algorithms and opted for an accurate editing of the raw data.

The amplitude spectrum of the data of both seismic lines shows a notch at about 75 Hz, possibly related to receiver ghost reflections. In fact, the notch frequency (Hz) of a receiver ghost reflection is given by (e.g. Provenzano et al., 2020)

$$f_n = V_w / \left(2 \times z_r\right), \quad (1)$$

where $V_w = 1.48$ km/s is the sea water velocity, and $z_r = 0.010$ km is the streamer depth (see also Table 1).

Figure 2 shows the reprocessed WEGA2601 and WEGA3501 seismic profiles, where the horizontal scale is given in CDP number and the vertical scale in two-way traveltime. De Santis et al. (2003) and Donda et al. (2003) provided exhaustive seismo-stratigrapic analysis and interpretation of the area. The sedimentary cover is characterized by three unconformities, namely WL-U6, WL-U7 and WL-U8, shown in Figure 2. In addition, on the basis of the seismo-stratigraphic evidence of the sequence between WL-U7 and WLU8, we introduce a new unconformity (WL-U7a). Further details about the geological meaning of these unconformities are given in the 'Sedimentological considerations and discussion' section.

13652478, 0, Downloaded from https://onlinelibrary.wiley.com/doi/10.1111/1365-2478.13425 by Ogs Trieste Istituto Nazionale, Wiley Online Library on [13/11/2023]. See the Terms and Conditions (https://onlinelibrary.wiley.com/terms-and-conditions) on Wiley Online Library for rules of use; OA articles are governed by the applicable Creative Commons License

## IODP SITE U1359

Site U1359 consists of four wells named A, B, C and D, reaching 193.50, 252.00, 168.70 and 602.2 meters below sea floor (mbsf), respectively (Figure 1). The dominant lithology observed throughout all holes is silty clay with dispersed clasts (Escutia et al., 2011). The only noticeable variations are the clast and diatom abundance, the amount of bioturbation, and the presence of dispersed packages of silt-fine sand laminations.

Downhole logging measurements were performed only at well D in the approximate depth-range of 104–602 mbsf. The log suites include several curves among which caliper, sonic, bulk density, porosity, gamma ray and resistivity. This study focuses on seismic-to-well tie; consequently, in our analyses, we consider only sonic and density logs. Three up-hole passes for the sonic profiles are available, whereas only one curve of the bulk density was acquired.

The four wells were cored with different coring systems and logged with the Whole-Round Multisensor Logger. The measurement included gamma ray attenuation, magnetic susceptibility, wet bulk density and P-wave velocity. According to micropaleontology and magnetostratigraphy analysis, the recovered successions span from late-middle Miocene to late Pleistocene (Tauxe et al., 2012). None of the two log datasets (wireline and core) provides continuous measurements of physical properties from the sea floor to the bottom of the deepest well D and consequently they must be integrated to obtain complete records.

## WIRELINE AND CORE LOGS EDITING, INTEGRATION AND UPSCALING

Well logs are influenced by borehole conditions which affect the quality of the measured properties. Density logs are sensitive to mud filtrate invasion or washout. Sonic logs can be affected by cycle skipping, seismic noise and tool problems (Gelpi et al., 2020). On the other hand, core logging can be affected by sample alteration, disturbance and deformation due to the changes in pressure and temperature at the core recovery or during the core cutting and handling (Riedel et al., 2006). This is particularly true in poorly consolidated sediments, like most of the vertical section of site U1359. Some log data-processing must be applied to both datasets in order to correct for unphysical values, manage depth intervals with missing measurements and make downhole and core logs comparable. In performing editing and corrections of well and core logs, we tried to be as much conservative as possible.

### Downhole logs

Among the relatively large suite of log measurements available from the well D of IODP site U1359, we consider the three velocity profiles obtained from three different up-hole passes and the bulk density curve. These measurements are called VCO1-3 and RHOM, respectively. The sampling interval of the wireline logs is 0.1524 m.

Despiking is the first well-log processing step we consider. In general, outliers in well-log curves can be caused by several factors, for example bad borehole conditions, ultra-thin beds, fractures corridors and cycle skipping (e.g. Bisaso, 2011; Lloyd & Margrave, 2013). The identification of unusual values in a dataset is a typical statistical problem. Assuming a normal distribution of data, a classic solution is based on the computation of the $z$-score, for example the distance, expressed in terms of standard deviation (SD), between each data value and the local mean (Rousseeuw & Hubert, 2011). Values with $z$-scores outside the range $\pm 3$ are considered outliers (Leys et al., 2013). Instead, we consider spikes the well-log values outside a range spanning 3 median absolute deviations (MAD) from the local median computed within a sliding window of 40 m (e.g. Bianco, 2014). Using the MAD with respect to the local median curve, instead of the SD from the local mean, preserves the procedure from being strongly affected by outliers (Leys et al., 2013; Rousseeuw & Hubert, 2011).

Once these spurious measurements are identified, they can be corrected with the methodology described in Bisaso (2011). Bad sections in the log curves can be replaced by realistic values or interpolated between the top and bottom of the interval. Alternatively, the bad log readings can be replaced with rock physical estimates from other logs. In this study, the spikes are removed and replaced with a cubic spline interpolation of nearby regular (non-outlier) entries.

An example of the despiking procedure applied to one of the three velocity logs (VCO2) and to the bulk density (RHOM) profile is illustrated in Figure 3.

The three velocity logs are very similar to each other, and we compute their average (arithmetic mean). Figure 4 shows the velocity logs from the three up-hole passes after despiking (VCO1-3) and the averaged curve (VCO).

### Core logs

Core logging data have been used for the uppermost portion of the sedimentary section, where wireline logs are not available. The four holes of site U1359 were cored in the following intervals: well A 0–190 mbsf, well B 8–242 mbsf, well C

13652478, 0, Downloaded from https://onlinelibrary.wiley.com/doi/10.1111/1365-2478.13425 by Ogs Trieste Istituto Nazionale, Wiley Online Library on [13/11/2023]. See the Terms and Conditions (https://onlinelibrary.wiley.com/terms-and-conditions) on Wiley Online Library for rules of use; OA articles are governed by the applicable Creative Commons License

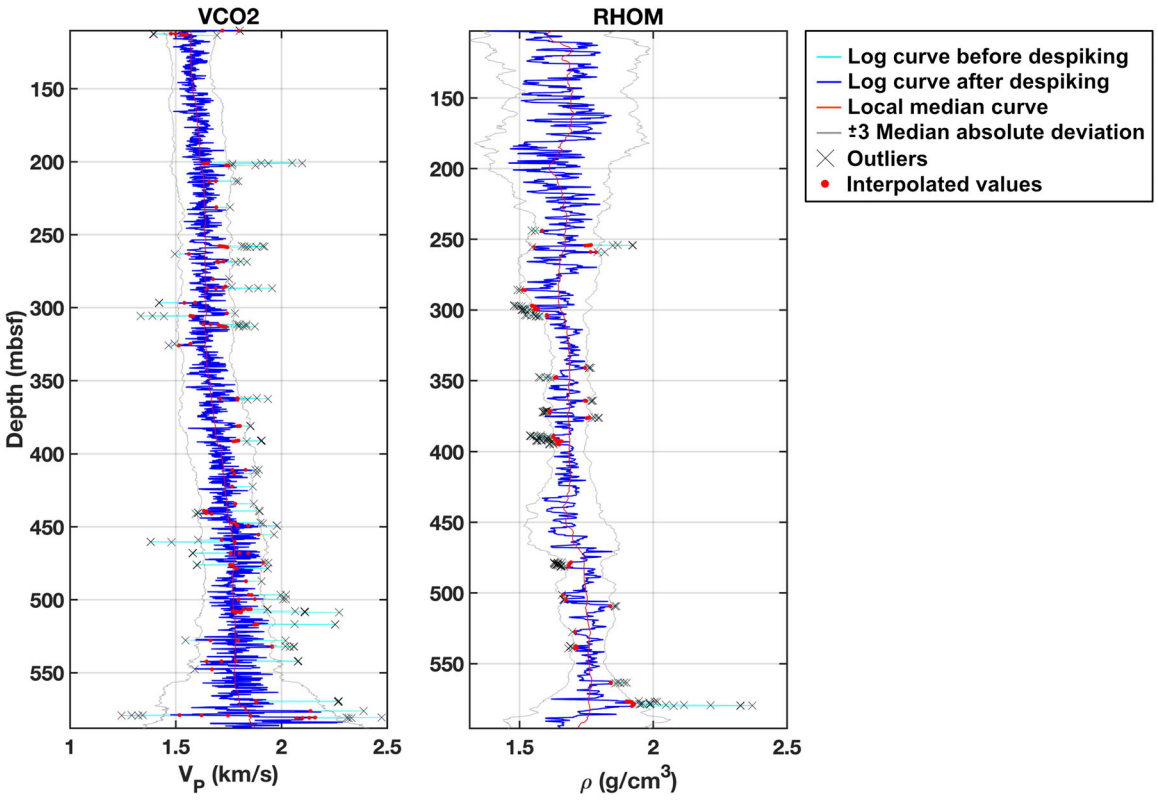


**FIGURE 3** Despiking procedure for the velocity (VCO2) and density profiles (RHOM). The blue curves represent the corrected log values, and the red curves are the median computed at the centre of a 40 m running window; the two thin black curves represent ±3 median absolute deviation (MAD), the black crosses are the values considered outliers and consequently removed and replaced by the values indicated by the red dots.

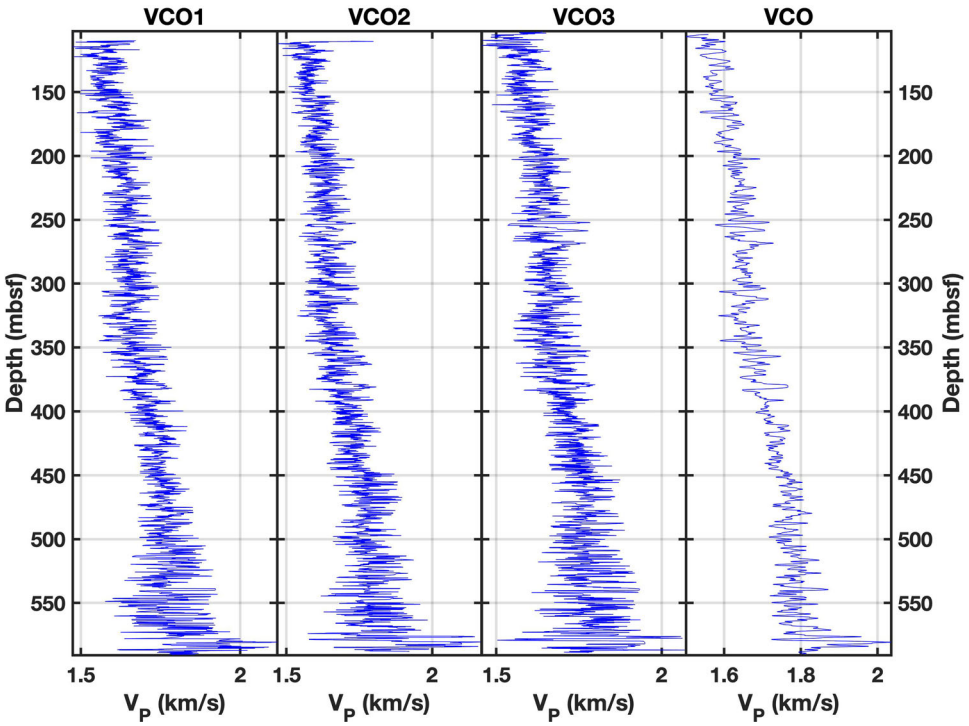


**FIGURE 4** Downhole velocity logs from three passes after despiking (VCO1-3) and the curve obtained from their arithmetic mean (VCO).

13652478, 0, Downloaded from https://onlinelibrary.wiley.com/doi/10.1111/1365-2478.13425 by Ogs Trieste Istituto Nazionale, Wiley Online Library on [13/11/2023]. See the Terms and Conditions (https://onlinelibrary.wiley.com/terms-and-conditions) on Wiley Online Library for rules of use; OA articles are governed by the applicable Creative Commons License

0–170 mbsf and well D 158–595 mbsf. The Advanced Piston Corer (APC) and the extended core barrel were used for wells A and B, whereas only APC was used in well C. The uppermost portion of well D was drilled using the Rotary Core Barrel system, and core was only recovered below 152.2 mbsf, where also more reliable wireline logs are available (Escutia et al., 2011). Accordingly, only core log data from wells A, B and C have been examined. Furthermore, in our computation, we consider relatively reliable the measurements from cores sections with recovery ratio of 90% or higher, discharging all the data not respecting these criteria.

Core logging was performed with the Whole-Round Multisensor Logger. This tool provides a very high vertical resolution but the measurements can be strongly influenced by ice-rafted debris, like isolated clasts. Moreover, core-based logging measurements assume the cross-sectional area of the sample to be constant. Different coring practices and unconsolidated sediments can fail this assumption causing erroneous measurements (e.g. Riedel et al., 2006).

The following properties were measured: magnetic susceptibility, natural gamma radiation, gamma ray attenuation bulk density (GRA) and P-wave logger velocity (PWL). For our analysis, we consider the curves GRA and PWL, having a sampling interval of 2.5 and 5 cm, respectively.

In order to make the core and wireline logs comparable, we resampled the former to the same logging rate of the latter. For each data point of the downhole logs, we consider the closest (in terms of depth) data points from the core logging and compute their arithmetic mean which will be located at that depth as a core log measure. Then, we apply the outliers removal procedure already described in the 'Downhole logs' section. Figure 5a shows the despiking of the core bulk density at well C. Interpolated values are marked by red points. Differently from the downhole log, the core logs show gaps in the curves due to the fact that we removed the data from sections of cores characterized by a recovery ratio lower than 90%. The despiking procedure interpolates the curves where outliers are removed but it does not act on log gaps. When the gaps are smaller than 10 samples (i.e. 1.5 m), we apply a linear interpolation to estimate the missing measurements: this is shown in Figure 5b where the red dots are the interpolated values. This procedure has been applied to the bulk density and P-wave velocity core measurements from the wells A, B and C.

The measurements from the three wells are characterized by a general agreement, even before data editing; however, local differences of up to 0.41 g/cm$^3$ and 100 m/s are observed, for density and P-wave velocity, respectively. These differences can be caused by the fact that the three wells are located a few 10th of meters apart and/or because the shallow sediments in this area are poorly consolidated and consequently affected by matrix disturbance and expansion during coring and retrieval. Due to these discrepancies, we do not average the three curves, but we use the measurements from well A integrated by the values from curve C to fill in gaps bigger than 1.5 m (A + C). We consider these two core log curves because they are the most complete from the sea floor to the beginning of the wireline logs at well D. Moreover, considering the combination A + C instead of C + A provides a slightly better result (higher cross-correlation coefficient) in the seismic-to-well tie procedure, described in the following sections.

Figure 6 shows the density profiles from core logging of the wells A, B and C and the curve GRA, obtained from merging the curves GRA_A and GRA_C, whereas Figure 7 shows the velocity profiles of the three wells and the log PWL obtained by merging the curves PWL_A and PWL_C.

## Logs integration and upscaling

We consider the wireline logs more reliable than the core dataset for representing the in situ conditions. In fact, the in situ physical properties of rock samples can be altered by the vibrations during coring and by the temperature and pressure variations after recovery and cutting. However, as wireline logs were not acquired in the cased section of the well from 0 to 104 mbsf approximately, we use core log measurements in this depth interval instead. Consequently, we merge the velocity curves PWL (0–105 mbsf) and VCO (105–590 mbsf); the same procedure is applied to the density curves GRA (0–104 mbsf) and RHOM (104–590 mbsf). We also upscale the log curves with a median filter over running windows of 6 m length. This procedure has the goal of relating fine-scale well-log measurements to coarser-scale seismic wavelengths (e.g. Bisaso, 2011).

Figure 8 shows the density (a) and velocity (b) curves obtained from the integration of the two logging methods. The reflectivity series shown in panel (d) was obtained by differentiating the acoustic impedance curve (Bianco, 2014). In the depth range between WL-U8 and WL-U7a, there is a clear correspondence between the high values of the reflectivity series ($R$) and the high amplitude reflection package in seismic data, suggesting that these amplitude anomalies are not a processing artefact but rather related to the actual physical properties of sediments.

# SYNTHETIC TRACE MODELLING

The main goal of the seismic-to-well tie is to relate the well-log data with field seismic sections through the modelling of a synthetic seismic trace. This latter is computed by convolving a wavelet representing the propagating seismic pulse with the reflectivity series obtained from the log data. This is a relatively well-established technique applied, possibly for the first

13652478, 0, Downloaded from https://onlinelibrary.wiley.com/doi/10.1111/1365-2478.13425 by Ogs Trieste Istituto Nazionale, Wiley Online Library on [13/11/2023]. See the Terms and Conditions (https://onlinelibrary.wiley.com/terms-and-conditions) on Wiley Online Library for rules of use; OA articles are governed by the applicable Creative Commons License

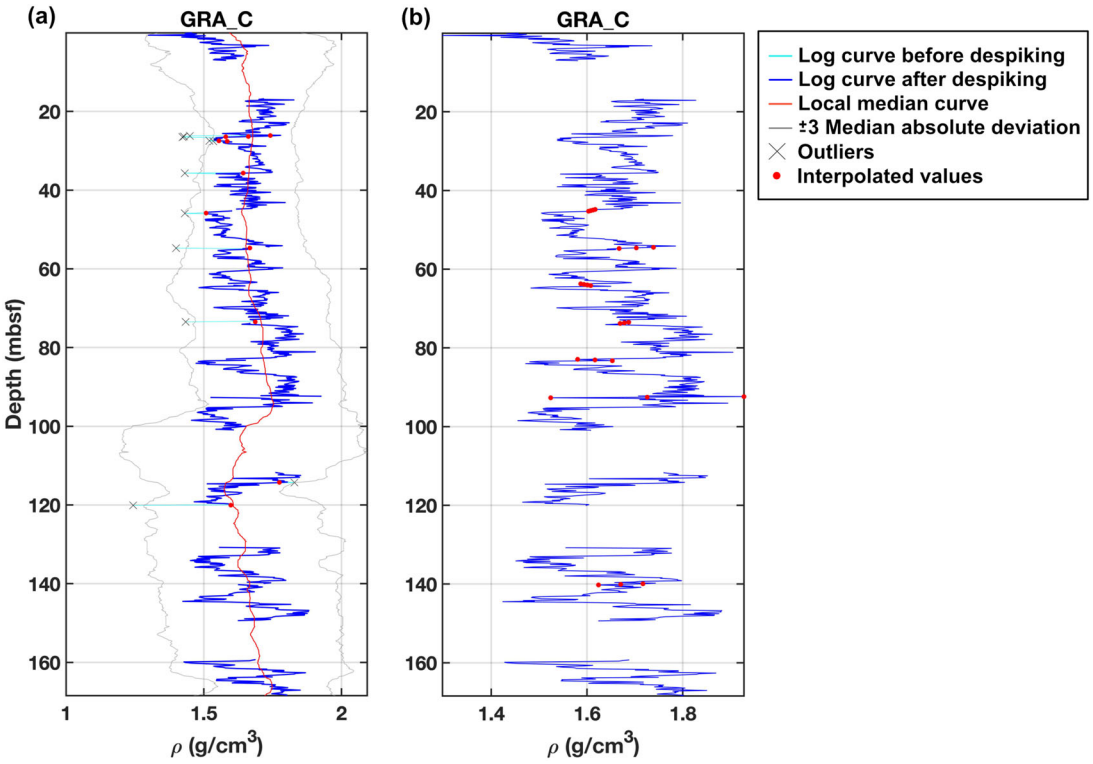


**FIGURE 5** (a) Despiking of bulk density measured from cores at hole C; (b) the curve shown in panel (a) after the filling gaps procedure, where the red dots are new samples obtained by linear interpolation.

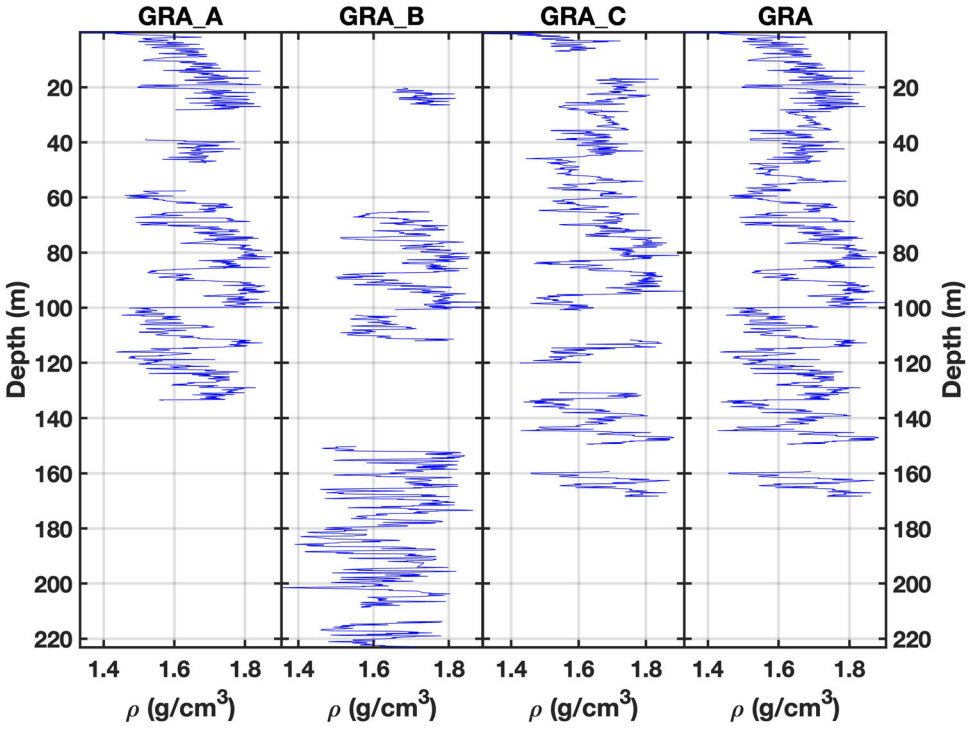


**FIGURE 6** Bulk density from core logging for hole A (GRA_A), hole B (GRA_B), hole C (GRA_C) and from merging the curves from holes A and C (GRA).

13652478, 0, Downloaded from https://onlinelibrary.wiley.com/doi/10.1111/1365-2478.13425 by Ogs Trieste Istituto Nazionale, Wiley Online Library on [13/11/2023]. See the Terms and Conditions (https://onlinelibrary.wiley.com/terms-and-conditions) on Wiley Online Library for rules of use; OA articles are governed by the applicable Creative Commons License

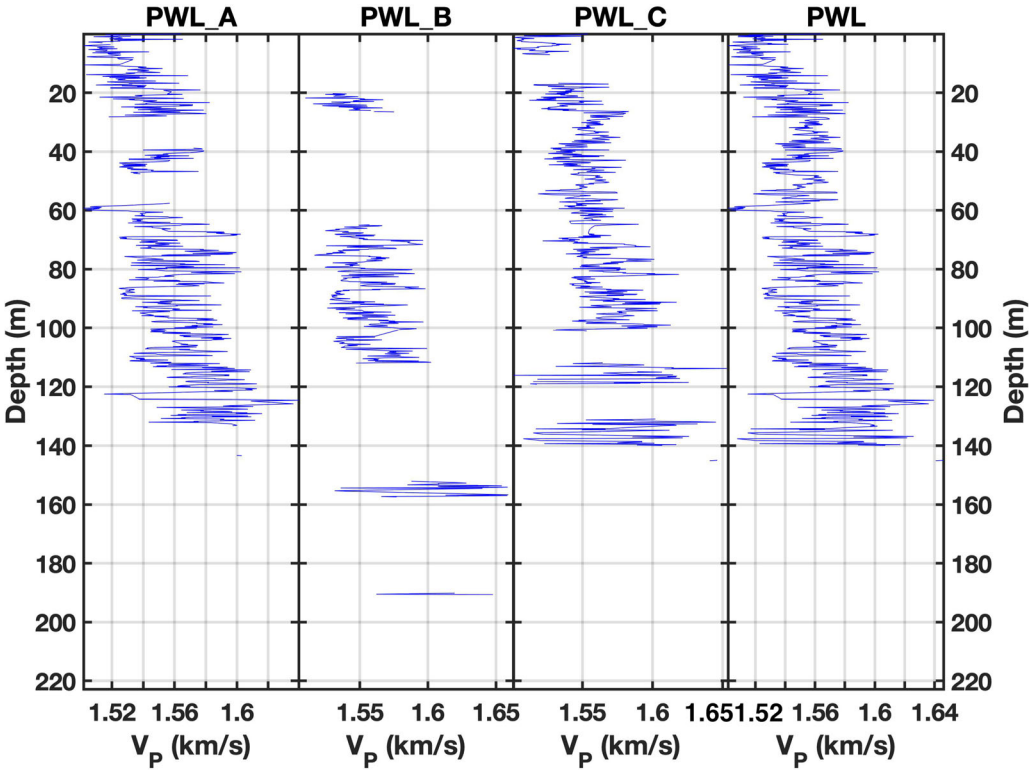


**FIGURE 7** P-wave velocity from core logging for hole A (PWL_A), hole B (PWL _B), hole C (PWL _C) and from merging curves of holes A and C (PWL).

time, by Peterson et al. (1955) and nowadays widely used for reservoir characterization in hydrocarbon exploration and in scientific studies. The synthetic trace is given by (e.g. White & Simm, 2003)

$$s\ (t) = R\,(t) \times w\,(t) + n\,(t)\,, \tag{2}$$

where $w(t)$ is the wavelet, and $n(t)$ is the noise. In this study, we neglect the influence of the noise and consequently assume $n(t) \approx 0$. $R(t)$ is the reflectivity series after depth–time conversion and resampling to $\mathrm{d}t = 2$ ms, the same sampling interval of the field seismic data. The depth–time relationship is computed by integrating the slowness along the depth vector $Z$ (e.g. Bader et al., 2019; Herrera et al., 2014):

$$T = 2 \int_Z \frac{\mathrm{d}z}{V_\mathrm{P}\,(z)}, \tag{3}$$

where $T$ is the two-way traveltime vector, and $V_\mathrm{P}(z)$ is the P-wave velocity log in depth below sea floor. The upscaling of the log curves to the seismic sampling interval $\mathrm{d}t$ is performed considering the average of the P-wave velocities and densities within each $\mathrm{d}t$ interval (Rietsch, 2021). We refer to $\tilde{T}$ as the resampled time vector $T$ and to $\tilde{Z}$ as the corresponding depth vector.

The sea-floor reflection is missing from the reflectivity series. In order to simulate such event, we compute the zero-offset reflection coefficient at the sea floor with (e.g. Yilmaz, 2001):

$$R_\mathrm{sf} = \frac{\rho_\mathrm{s} V_\mathrm{s} - \rho_\mathrm{w} V_\mathrm{w}}{\rho_\mathrm{s} V_\mathrm{s} + \rho_\mathrm{w} V_\mathrm{w}}, \tag{4}$$

where $\rho_\mathrm{w}$ and $\rho_\mathrm{s}$ are the densities of the sea water and sediments, respectively, and $V_\mathrm{w}$ and $V_\mathrm{s}$ are the corresponding P-wave velocities. $V_\mathrm{w} = 1.48$ km/s is estimated from the velocity analysis of the WEGA seismic lines and is confirmed by the RAE stack velocities, whereas $\rho_\mathrm{w} = 1.028$ g/cm$^3$ (Wong & Riser, 2011). The seismic properties of the sediments are computed considering the mean of the density and velocity curves shown in Figure 8, panels (a) and (b), in the range 0–40 mbsf. We obtain $\rho_\mathrm{s} = 1.65$ g/cm$^3$ and $V_\mathrm{s} = 1.538$ km/s, and consequently $R_\mathrm{sf} = 0.25$. $R_\mathrm{sf}$ is not shown in Figure 8d and will constitute the first sample of the reflectivity series used to compute the synthetic trace.

A fundamental step in modelling the synthetic trace is the definition of the seismic wavelet to be convolved with the reflectivity series. The wavelet is generally estimated from the seismic data only (statistical methods) or using also well-log data (deterministic methods) (e.g. de Macedo et al., 2017).

13652478, 0, Downloaded from https://onlinelibrary.wiley.com/doi/10.1111/1365-2478.13425 by Ogs Trieste Istituto Nazionale, Wiley Online Library on [13/11/2023]. See the Terms and Conditions (https://onlinelibrary.wiley.com/terms-and-conditions) on Wiley Online Library for rules of use; OA articles are governed by the applicable Creative Commons License

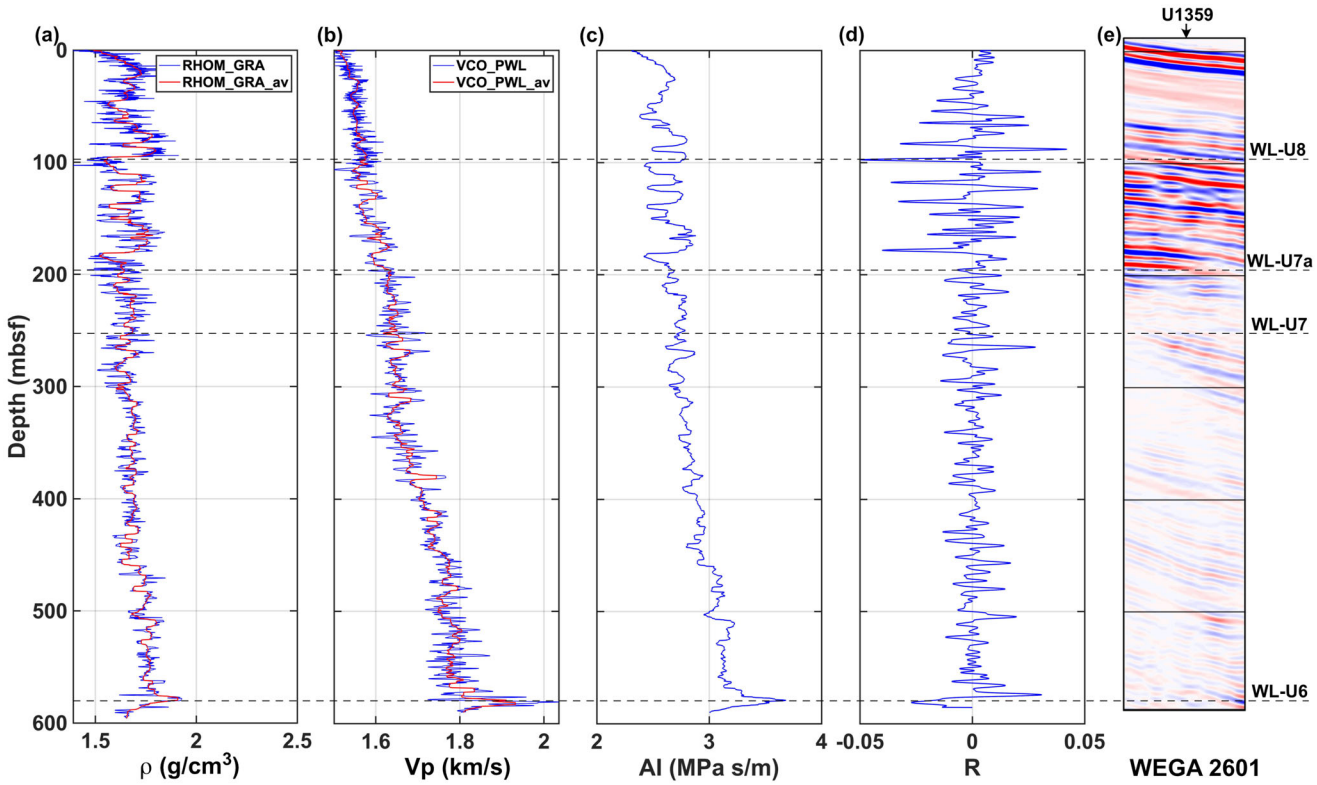


**FIGURE 8** Density log (a) and velocity log (b) from the integration of downhole and core logs before (blue) and after (red) upscaling, acoustic impedance (c) computed from the product of the curves RHOM_GRA_av and VCO_PWL_av, reflectivity series (d) and part of the section WEGA2601 centred at the well site and converted to depth with the upscaled velocity curve (VCO_PWL_av) (e); the depths of the main unconformities are also indicated.

Another option is the use of the sea-floor reflection extracted from seismic traces located in proximity of the well head. This wavelet can be as good as wavelets estimated with more complex methods like spectral division or least-square fit (Bo et al., 2013). As described in 'Wavelet estimation' section, we considered two different wavelets for the two seismic sections obtaining two synthetic traces from the same reflectivity series.

## SEISMIC-TO-WELL TIE PROCEDURE

The classical seismic-to-well tie process is described in several papers (e.g. Bianco, 2014; Bianco, 2016; White & Simm, 2003), as well as the pitfalls hidden in the procedure (Anderson & Newrick, 2008). Theoretically, the synthetic trace should be compared with the seismic trace closest to the well. However, log data at site U1359 are obtained by integrating the data from three different holes, and consequently, it is not possible to define the seismic traces closest to the well location. Moreover, the seismic data migration process can move the best match location away from the well (Herrera & van der Baan, 2014). Therefore, following White and Simm (2003), we scan an interval of traces of the seismic lines in the vicinity of the well heads to find the best matching location. We then quantify the likeness of the synthetic and experimental seismic traces with two standard methods: the correlation coefficient (CC) and the proportion of trace energy (PEP) (e.g. Bianco, 2016; Simm & Bacon, 2014). These two measures of goodness-of-fit are described in Appendix A.

The matching is applied independently on the two seismic sections in proximity of the holes and specifically in the common depth point (CDP) ranges 2813–2865 (SP 787-800) for the line WEGA2601 and 6525–6577 (SP 1717-1730) for the line WEGA3501 (see Figure 1). The procedure consists in:

- the extraction of the sea-floor reflection from the experimental seismic trace, to be used as wavelet for the synthetic trace;
- the convolution of the wavelet with the reflectivity series in time to obtain the synthetic trace;
- the alignment of the synthetic and field trace by a cross-correlation procedure;
- the computation of CC and PEP with the actual seismic and synthetic traces.

13652478, 0, Downloaded from https://onlinelibrary.wiley.com/doi/10.1111/1365-2478.13425 by Ogs Trieste Istituto Nazionale, Wiley Online Library on [13/11/2023]. See the Terms and Conditions (https://onlinelibrary.wiley.com/terms-and-conditions) on Wiley Online Library for rules of use; OA articles are governed by the applicable Creative Commons License

The success of the seismic-to-well tie depends on the quality of the well logs and seismic data and on the processing of both datasets, on the estimation of a proper wavelet for computing the synthetic trace, as well as on the correct timing of the synthetic trace (Herrera & van der Baan, 2014; Herrera et al., 2014; Lloyd & Margrave, 2013; White & Simm, 2003). Log measurements probe the rocks with signals having a frequency of a few 10th of kHz, whereas the amplitude spectrum of the raw seismic data considered in this study rapidly decays after 150 Hz. The velocity of propagation of compressional waves in sediments increases with the frequency of the signal (e.g. Gei & Carcione, 2003; Sams et al., 1997). This difference causes discrepancies between the sonic times and seismic times which can be corrected with a well-log calibration procedure when check shot or vertical seismic profile (VSP) data are available (e.g. Lloyd & Margrave, 2013; White & Simm, 2003).

The planned VSP survey at site U1359, well D, failed for instrumentation malfunctioning. Only four waveforms have been recorded with the receiver resting at the bottom of the hole, at 601.5 mbsf, but they result in quite different one-way traveltimes making this data unreliable. Consequently, we did not apply the check shot calibration, opting instead for a cross-correlation based technique to be applied on the synthetic trace (Cui & Margrave, 2015), as described in 'Mis-ties correction' section. This choice was supported by the good correlation between the strong velocity variation at about 580 mbsf (Figure 8b) and a prominent seismic unconformity (WL-U6).

## Wavelet estimation

The seismic wavelet to be used for modelling the synthetic seismic trace is the sea-floor reflection extracted from experimental seismic traces in proximity of the well's locations. The wavelets providing the best results are shown in Figure 9, together with their amplitude and phase spectra: The notch at about 75 Hz can be clearly identified. As already mentioned in the 'Processing of legacy seismic data' section, this frequency notch is related to the receivers' ghost effect. Using a notch-affected wavelet for computing the synthetic trace is consistent with the processing sequence applied to the seismic data, which do not include any ghost-correction procedure.

For the line WEGA2601, we obtain the highest goodness-of-fit at CDP 2848 (SP 796 approximately) close to well D. Instead, for the line WEGA3501, the highest goodness-of-fit is obtained at CDP 6540 (SP 1721). The locations of the field traces best matching the synthetics are indicated by red stars in Figure 1.

The blue and red traces in panels (a) and (c) of Figure 10 represent the best matching field and synthetic traces for the two lines. Considering the whole length of the synthetic trace, we obtain CC = 0.72 and PEP = 0.51 for WEGA2601 (panel a) and CC = 0.76 and PEP = 0.58 for WEGA3501 (panel c). For both seismic lines, synthetic and field traces agree in their general character especially in the time range 4.15–4.40 s, corresponding to the high amplitude reflection package indicated in Figure 2. At higher two-way traveltime (twt), the amplitude of the field traces drastically reduces if compared with the synthetics, possibly due to intrinsic attenuation.

We also applied a more classic wavelet estimation method, falling into the category of the statistical methods (e.g. Bo et al., 2013). We computed minimum phase wavelets with the amplitude spectrum obtained from the autocorrelation function of the seismic traces closer to the wells after applying a predictive deconvolution to the two seismic datasets, but we obtained poorer results in the seismic-to-well tie procedure. This result is due to a poor estimation of the wavelet and confirms that using the sea-floor reflection in modelling the synthetic trace is a good option, at least for this specific dataset.

## Mis-ties correction

Mis-ties are quite common in core-log-seismic integration and can be due to several factors such as bad hole conditions influencing the log readings or subjectivities in the data processing. The simple forward modelling procedure we applied assumes zero-offset and noise-free seismic data, and migration artefacts or other form of noise (e.g. seismic multiples) cannot be reproduced in the synthetic trace (e.g. Cui, 2015). Moreover, we consider stationary wavelets and consequently neglect attenuation and dispersion effects. These aspects may contribute to possible mismatching between synthetic and experimental seismic traces, whatever wavelet is used (Anderson & Newrick, 2008; Cho & Nordin, 2014; Herrera & van der Baan, 2014; Margrave, 2013). For this study, mis-ties can also be related to the impossibility to perform the check-shot calibration of the log data.

When check shot data and Q information are not available, synthetic seismograms can be stretched or squeezed to reduce the mis-tie and increase the goodness-of-fit measures (Cui & Margrave, 2015; Gelpi et al, 2020; Lloyd & Margrave, 2013). This practice can be arbitrary, often not supported by strong geological/geophysical evidence and consequently criticized by some authors (e.g. Cho & Nordin, 2014; White & Simm, 2003), but it has become a common tool in modern seismic interpretation and inversion software (Bader et al., 2019; Zhang et al., 2020). If accompanied by the unshifted seismograms and limited in the magnitude of the applied time shifts, it can be a useful tool for interpreters.

Traditionally, the procedure of stretching and squeezing the synthetic trace was operated manually by the interpreter. However, in the last few decades, with the aim of limiting human errors, several automatic methods have been proposed,

13652478, 0, Downloaded from https://onlinelibrary.wiley.com/doi/10.1111/1365-2478.13425 by Ogs Trieste Istituto Nazionale, Wiley Online Library on [13/11/2023]. See the Terms and Conditions (https://onlinelibrary.wiley.com/terms-and-conditions) on Wiley Online Library for rules of use; OA articles are governed by the applicable Creative Commons License

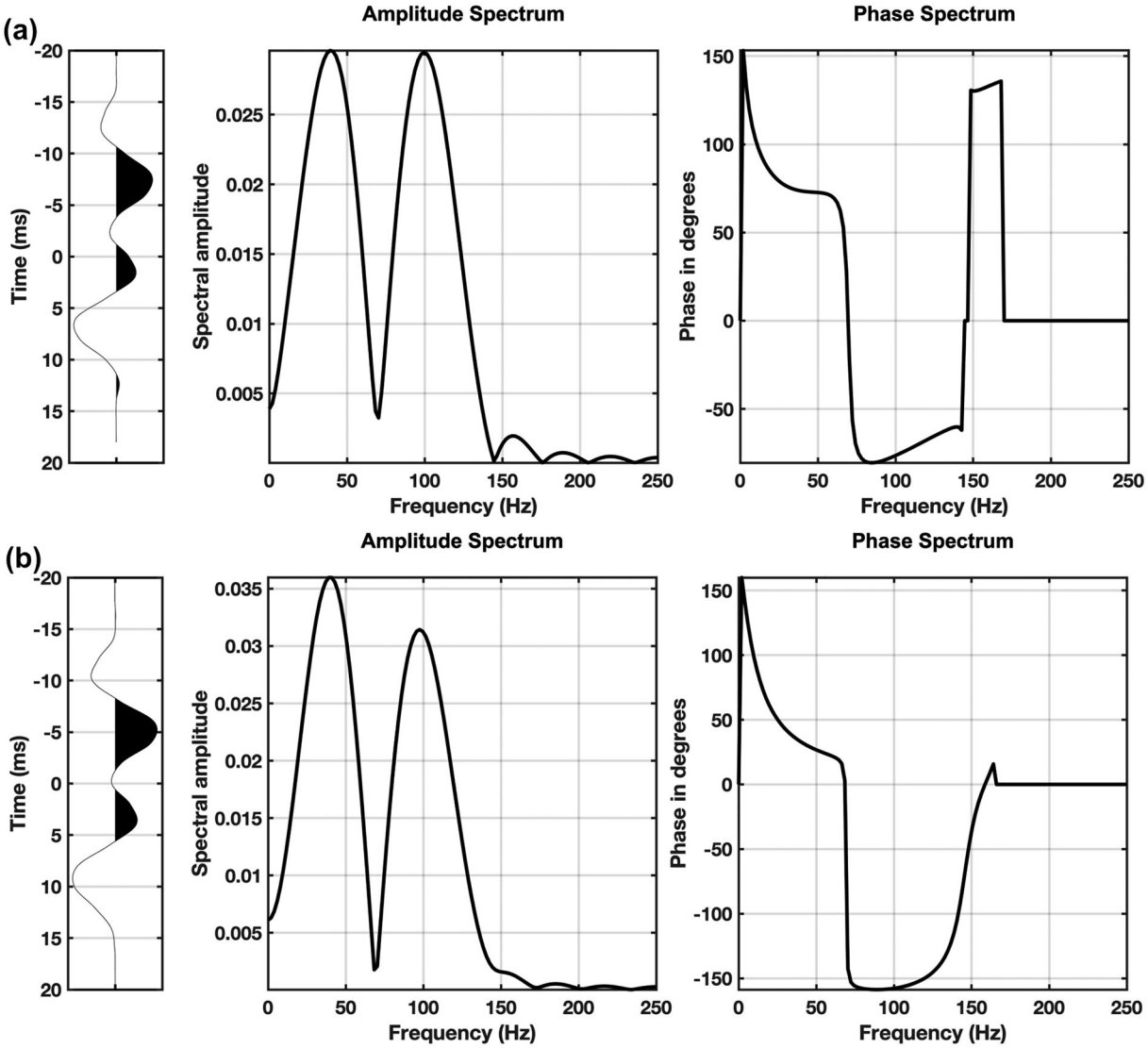


**FIGURE 9** The wavelets used for computing the synthetic traces for the seismic lines WEGA2601 (a) and WEGA3501 (b) and their amplitude and phase spectra; they are the sea-floor reflections of common depth points (CDPs) 2848 and 6540, respectively.

for example the dynamic time warping (DTW) (Cui & Margrave, 2015; Herrera et al., 2014; Zhang et al., 2020) or the local similarity attribute (Bader et al., 2019; Fomel, 2007; Herrera et al., 2014). In this study, we consider the time variant cross-correlation (TVCC) filter, based on sliding time windows of constant size (Cho, 2013; Cui & Margrave, 2015). This method is suitable for slow-varying time shifts, whereas others, like the DTW, are preferable in the case of high shift rates (Cui & Margrave, 2015). Like other automatic methods, TVCC has the advantage of reducing the interpreters' bias, still controlling the squeezing and stretching applied to the synthetic trace. The TVCC technique is described in Appendix B. We applied the TVCC filter to both synthetic traces, with the following input parameters: Gaussian time window of 70 ms half-width, lag time $t_{\text{lag}} = 4$ ms and windows time shift interval $\tau = 50$ ms.

Considering the line WEGA2601, the time shift curve shown in Figure 10b is applied to the synthetic trace shown in panel (a), resulting in the synthetic shifted trace. Thanks to these stretching and squeezing the synthetic shifted trace shows a better matching with the field trace. The same considerations can be done for the traces and time shift of line WEGA3501 shown in panels (c) and (d), respectively. The goodness-of-fit improved considerably, resulting in CC = 0.79, PEP = 0.62 and CC = 0.81, PEP = 0.66 for WEGA2601 and WEGA3501, respectively.

Dispersion effects due to the different frequencies involved in the log and seismic measurements and intrinsic attenuation of the field data should decrease the P-wave velocity of the seismic pulse, increasing the twt. Unexpectedly, even considering a wide range of the input parameters, the TVCC procedure leads to an overall squeezing of the synthetic

13652478, 0, Downloaded from https://onlinelibrary.wiley.com/doi/10.1111/1365-2478.13425 by Ogs Trieste Istituto Nazionale, Wiley Online Library on [13/11/2023]. See the Terms and Conditions (https://onlinelibrary.wiley.com/terms-and-conditions) on Wiley Online Library for rules of use; OA articles are governed by the applicable Creative Commons License

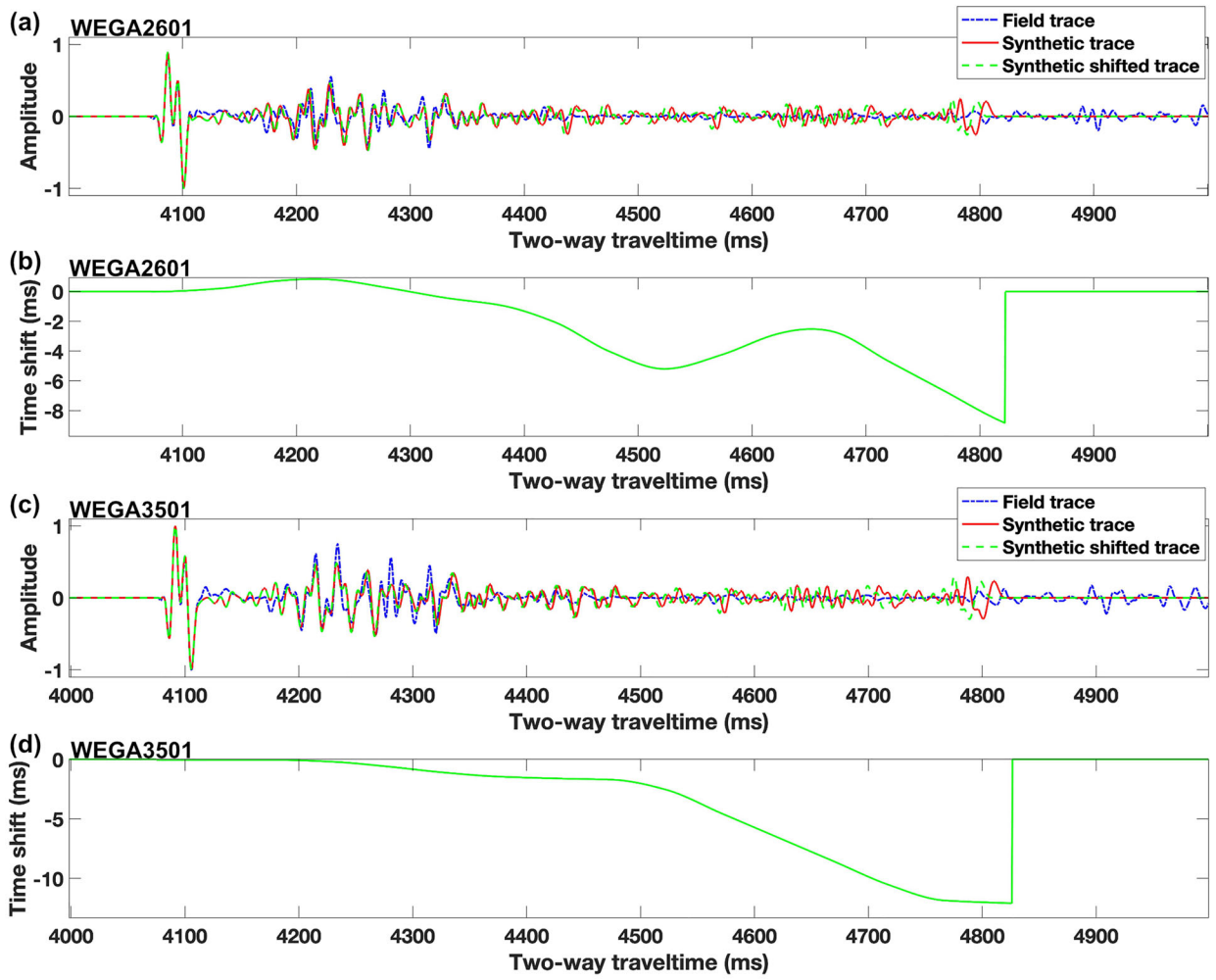


**FIGURE 10** Field trace and synthetic trace before and after the application of the time shift for the lines WEGA2601 and WEGA3501, (a) and (c) respectively, and the corresponding time shifts, (b) and (d).

trace which causes a general increase of the seismic velocity. This aspect might be deeply investigated by analysing check shot survey datasets, unfortunately not available for this site.

The results of the seismic-to-well tying for the lines WEGA2601 and WEGA3501 are also shown in Figures 11 and 12, respectively. There is a general good agreement of synthetic and experimental data, in terms of polarities and amplitudes, especially for seismic events between the unconformities WL-U8 and WL-U7.

Stretching and squeezing the synthetic seismic trace produce a better tie but also results in waveform deformation and modification of the P-wave seismic velocity profile (Gelpi et al., 2020). The choice of the TVCC filter input parameters compromises between the increasing of the goodness-of-fit and abrupt variations of the time shift function $t_{\mathrm{shift}}$, which strongly influence the modified P-wave velocity curve. It is important to verify the reliability of these perturbed velocities to avoid unphysical situations (Bader et al., 2019; Herrera et al., 2014). The P-wave velocity profile modified by the time shifting of the synthetic trace can be obtained from (Bader et al., 2019):

$$V_{\mathrm{P}}^{\mathrm{st}}\left(\tilde{Z}\right) = V_{\mathrm{P}}\left(\tilde{Z}\right)\left(\frac{\mathrm{d}t_{\mathrm{shift}}}{\mathrm{d}t} + 1\right)^{-1}, \tag{5}$$

where $V_{\mathrm{P}}(\tilde{Z})$ is the P-wave log velocity, and $t_{\mathrm{shift}}(\tilde{T})$ is the time shift to be applied to the synthetic trace, resulting from the TVCC procedure. Figure 13 shows the P-wave velocity log $V_{\mathrm{P}}(Z)$, the same profile after resampling $V_{\mathrm{P}}(\tilde{Z})$ and the velocities modified by the time shifting $V_{\mathrm{P}}^{\mathrm{st}}(\tilde{Z})$ applied to the synthetic traces. The higher velocity perturbations are 4.43% for WEGA2601 and 4.54% for WEGA3501. These values result in negligible differences when computing the depth of seismic events with depth–time relationships obtained with $V_{\mathrm{P}}(\tilde{Z})$ or $V_{\mathrm{P}}^{\mathrm{st}}(\tilde{Z})$; specifically, we obtain a difference of less than 2 m for reflectors above 4.4 s (twt of WL-U7, base of the high amplitude reflection package) and a maximum of 10 m for the reflector at about 4.8 s.

13652478, 0, Downloaded from https://onlinelibrary.wiley.com/doi/10.1111/1365-2478.13425 by Ogs Trieste Istituto Nazionale, Wiley Online Library on [13/11/2023]. See the Terms and Conditions (https://onlinelibrary.wiley.com/terms-and-conditions) on Wiley Online Library for rules of use; OA articles are governed by the applicable Creative Commons License

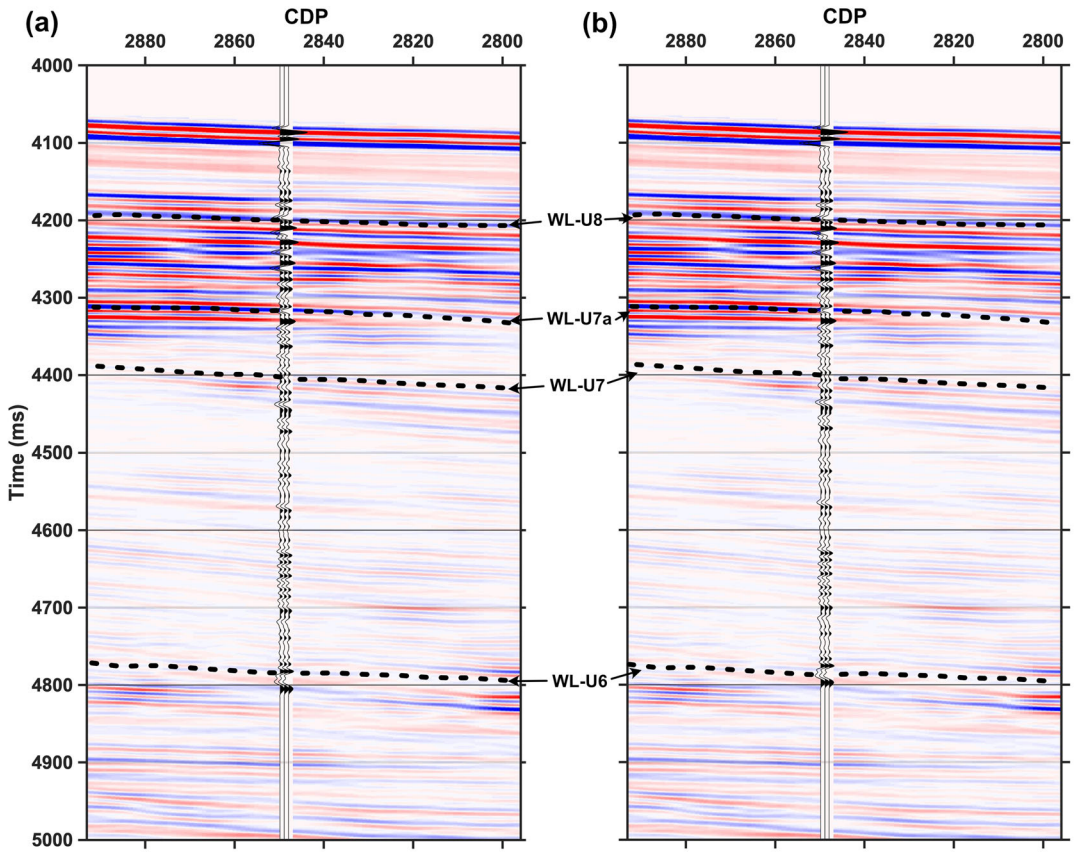


**FIGURE 11** Superposition of the seismic section WEGA2601 in variable density and three synthetic traces in wiggle-variable area before (a) and after (b) the application of the time variant cross-correlation (TVCC) filter; the main unconformities characterizing the area are also indicated.

**TABLE 2** Summary of the seismic unconformities; depths and two-way times (twt) are referred to the site 1359.

| Name | twt (ms) | twt (ms) below sea floor | Depth (m) below sea floor |
|---|---|---|---|
| WL-U8 | 4200 | 124 | 98 |
| WL-U7a | 4320 | 240 | 192 |
| WL-U7 | 4400 | 320 | 253 |
| WL-U6 | 4780 | 700 | 580 |

## SEDIMENTOLOGICAL CONSIDERATIONS AND DISCUSSION

The seismic-to-well tie allows us to correctly estimate the depth of the main seismic features, for example seismic unconformities, and test their correspondence with the main lithostratigraphic units and with the main petrophysical changes in the sediments. Considering the water depth (3000–3500 m) and the short-offset of the seismic data, the velocity that can be obtained from the seismic data processing is not reliable and the calibration with the well logs is the only way to define a robust depth–time relationship. For this purpose, we use the Equation (3) and the upscaled P-wave seismic velocity shown in Figure 8. The results are summarized in Table 2.

The sediments cored at site U1359 consist of silty clays with dispersed clasts. Based on the style of laminations, bioturbation, or the relative abundance of the biogenic versus terrigenous component, Escutia et al. (2011) identified three lithostratigraphic units (Units I, II and III). Moreover, Unit II has been split into three sub-Units: IIa, IIb and IIc. The depths of the seismic unconformities reported in Table 2 allow us to link those seismic features to the lithostratigraphic units and to estimate their age (Figure 14): The age of WL-U6 is 13 Ma, WL-U7 is 9 Ma, WL-U7a is 6.5 Ma, and WL-U8 is about 4.5 Ma.

13652478, 0, Downloaded from https://onlinelibrary.wiley.com/doi/10.1111/1365-2478.13425 by Ogs Trieste Istituto Nazionale, Wiley Online Library on [13/11/2023]. See the Terms and Conditions (https://onlinelibrary.wiley.com/terms-and-conditions) on Wiley Online Library for rules of use; OA articles are governed by the applicable Creative Commons License

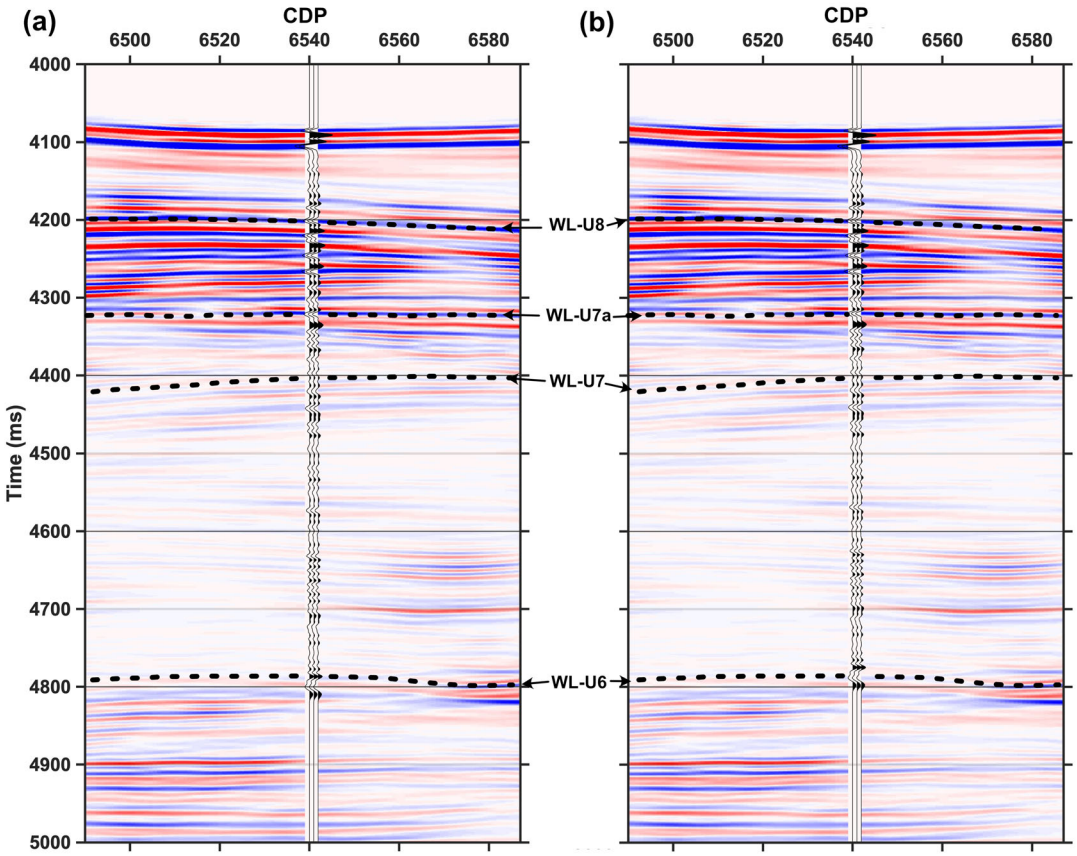


**FIGURE 12** Superposition of the seismic section WEGA3501 in variable density and three synthetic traces in wiggle-variable area before (a) and after (b) the application of the time variant cross-correlation (TVCC) filter; the main unconformities characterizing the area are also indicated.

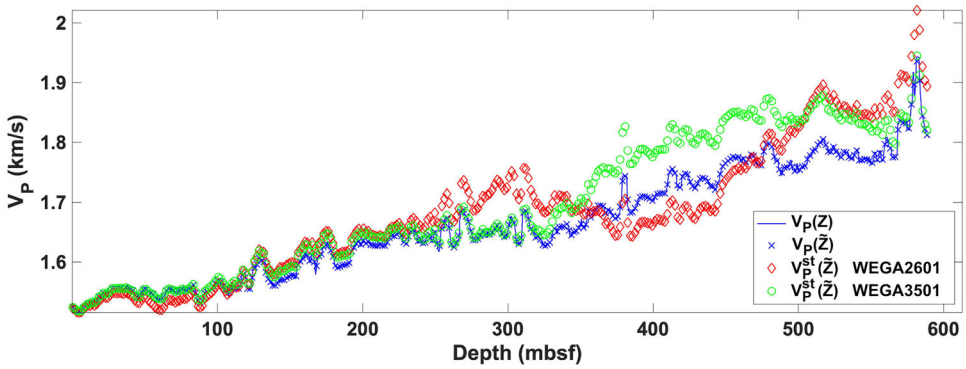


**FIGURE 13** Comparison between the original and time-shift-modified P-wave velocity for the lines WEGA2016 and WEGA3501.

A first observation resulting for the depth conversion of the seismic unconformities regards the sedimentation rate of the sub-Unit IIc. According to Tauxe et al. (2012), the highest values (101 m/Ma) occurred during the deposition of the lithological unit IIb, corresponding to the interval between WL-U8 and WL-U7a; the same sedimentation rate characterizes the Unit III (WL-U7–WL-U6) (Figure 14). Instead, much lower rates (18 m/Ma) characterize Unit IIc that roughly corresponds to the interval between WL-U7 and WL-U7a. From Figure 2, line WEGA3501, we can observe that the thickness of Unit IIc (between WL-U7a and WL-U7) at well location is at a local minimum, due to the presence of a sediment wave. Considering the average sediment thickness of the seismic interval WL-U7a–WL-U7 out of the well location, the sedimentation rates for Unit IIc could have been at least twice the 18 m/Ma of Tauxe et al. (2012).

13652478, 0, Downloaded from https://onlinelibrary.wiley.com/doi/10.1111/1365-2478.13425 by Ogs Trieste Istituto Nazionale, Wiley Online Library on [13/11/2023]. See the Terms and Conditions (https://onlinelibrary.wiley.com/terms-and-conditions) on Wiley Online Library for rules of use; OA articles are governed by the applicable Creative Commons License

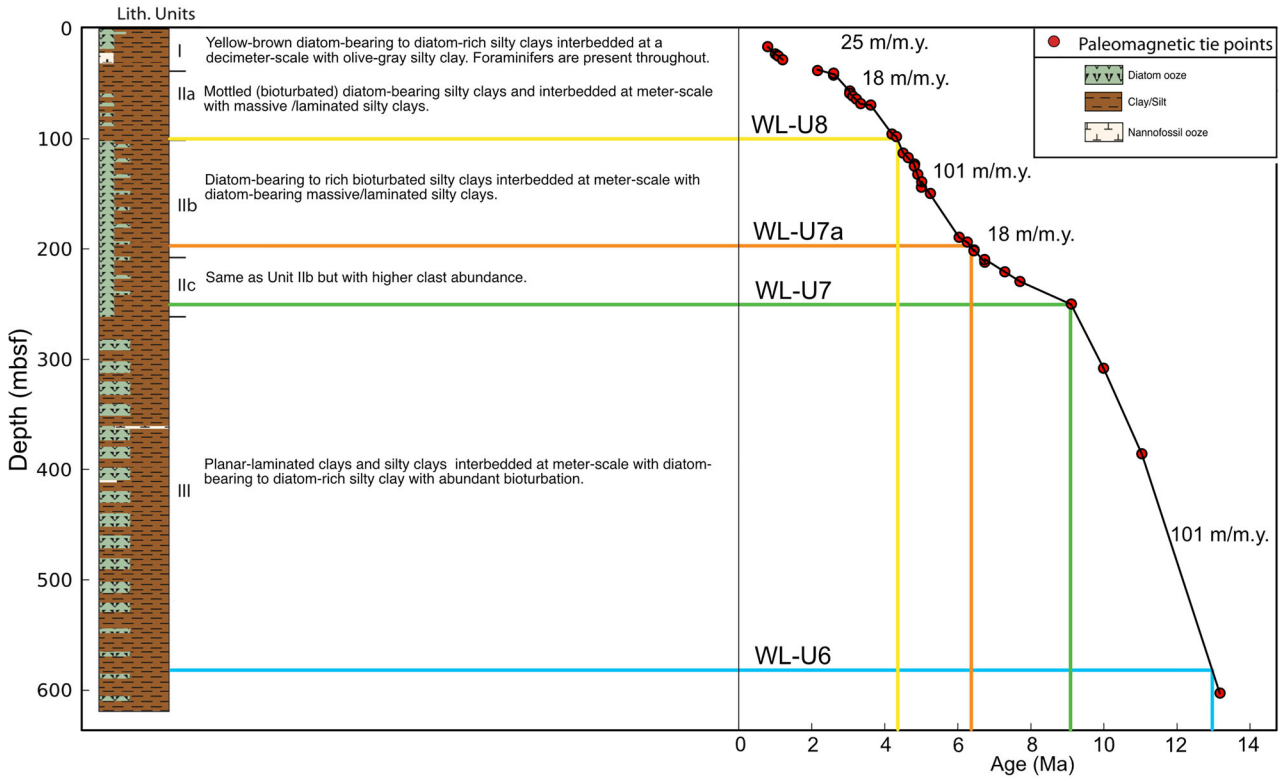


**FIGURE 14** Age-depth plot with the main seismic unconformities (WL-U6, -U7, -U7a, -U8), the sediment composition, the lithostratigraphic units with descriptions and sedimentation rates. *Source*: Modified after Escutia et al. (2011) and Tauxe et al. (2012).

A second important observation regards the composition of the sedimentary sequence and its influence on the seismic images. The sub-Units IIb and IIc roughly correspond to the interval between unconformities WL-U7 and WL-U8 and show a relatively high diatom content. WL-U7 marks the base of a seismic unit with parallel, laterally continuous, high amplitude reflectors (Figure 2). The bottom of this seismic facies characterizes younger units at the northern and upper portion of the eastern levee of the Jussieu channel, and it is bounded at the top by WL-U8, which crosses site U1359 at 4200 ms two-way traveltime. This analysis suggests a possible relationship between the diatom fraction in the sediments and the high amplitude reflections.

Figure 15 shows the biogenic and terrigenous fractions from Escutia et al. (2011) and the diatoms content from Khim et al. (2017), together with the velocity and density core-log measurements from the well A at site U1359; the right panel is the reflectivity ($R$) computed at seismic resolution with the velocity and density curves. The choice of the logs from a single well rather than from the cumulative log is due to the opportunity to have a one-to-one relationship between logs and lithology.

Due to the presence of large gaps inside the recovered cores, the analysed section is limited to 60 m, of which only 35 m represent the high amplitude seismic unit we are analysing. Unfortunately, there is no possibility to enlarge a reliable analysis to other depths of holes as all the other wells present relevant gaps in recovery or log data. On the other hand, due to the regularity of the sedimentation between WL-U8 and WL-U7 (i.e. Units IIb and IIc in Figure 14), we believe that

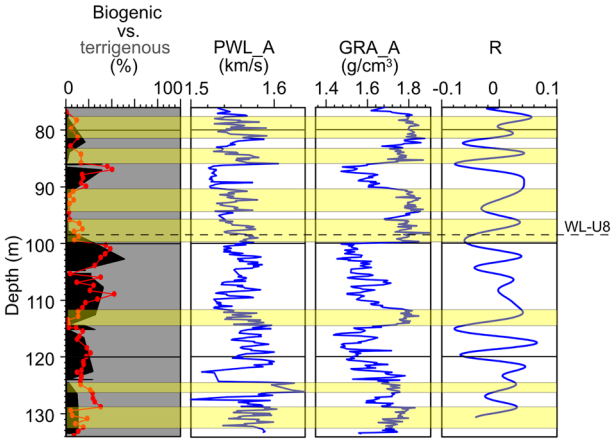


**FIGURE 15** Correlation between sediments composition (biogenic and terrigenous fractions) from Escutia et al. (2011), diatoms content (red dots) from Khim et al. (2017), P-wave velocity (PWL_A) and density (GRA_A) of well A, and the reflectivity series $R$ obtained from these velocity and density curves; the yellow horizontal bands highlight the high density packages that correlate with lower percentages of diatoms and with positive peaks of the reflectivity.

13652478, 0, Downloaded from https://onlinelibrary.wiley.com/doi/10.1111/1365-2478.13425 by Ogs Trieste Istituto Nazionale, Wiley Online Library on [13/11/2023]. See the Terms and Conditions (https://onlinelibrary.wiley.com/terms-and-conditions) on Wiley Online Library for rules of use; OA articles are governed by the applicable Creative Commons License

the analysed section can be considered quite representative of our area of interest.

Figure 15 highlights the fairly good correlation among high density, relatively high velocity packages and the low percentages (less than 10%) or absence of the biogenic component (diatom). The reflectivity series in Figure 15 is therefore related to the variation of the biogenic component of the sediment. We believe that this relationship could be the product of two different processes (1) a much lower density of the diatom rich sediments compared to the silt/clay sediments, (2) the presence of a disequilibrium in the compaction curve (Dasgupta & Mukherjee, 2020; Schwehr et al., 2006). Volpi et al. (2003) observed that intergranular contacts among diatoms prevented normal sediment consolidation in the sediment of another sector of the Antarctic continental margin, under conditions of pressure and diagenesis similar to those present at site U1359. Those authors also observe that the influence of diatom microstructure on physical properties can be appreciated at low diatom contents (<20 wt%) in natural clay-rich marine sediments. This would support the hypothesis (1), for explaining the low- and high-density packages with diatom percentage change, above and below 10%. Hypothesis (2) has been already suggested by Escutia et al. (2011) to account for the variations in the magnetic anisotropy degree at site U1359. In this case, compaction disequilibria could be produced by differences in excess pore water caused by the more clay-rich versus more diatom-rich layers (Schwehr et al., 2006). Geotechnical analysis, out of the scope of this article, is needed to test these hypotheses.

The high amplitude, laterally continuous, sub-parallel reflectors that characterize the seismic unit between WL-U8 and WL-U7a correlate well with sudden changes in acoustic impedance and reflection coefficient (Figure 8). These changes presumably correspond to large density variations in the log of well A, with frequency of about 5 m and highlighted in Figure 15 by yellow bands. These density changes can produce high amplitude reflections in the seismic profiles used in this study that has a vertical resolution of 5 m, approximately.

The section above WL-U8 has semi-transparent acoustic character (Figure 2), which is in agreement with its overall lower reflectivity (Figure 8), and with a generally high density and a lower content of biogenic silica at well A (Figure 15), comparing to the section below WL-U8.

The results of this work demonstrate the relationship between seismic amplitude anomalies and presence of alternated layers of diatom-rich to silty/clay strata from late Miocene-early Pliocene at Integrated Ocean Drilling Program site U1359. The top and bottom of these layers correspond to sharp density changes that originate seismic reflections clearly detected by high-resolution seismic profiles. The age of this sedimentary package corresponds to the main phase of development of the Antarctic Ice Sheet and the alternation of the diamicton/diatom rich sediments can be interpreted as reflecting ice sheet growth/retreat during climate cycles. The analysis of other sites from the Antarctic continental rise can then be used as a proxy for the presence of a peculiar sedimentary section, indicative of major palaeoclimatic and palaeoceanographic changes at the transition from temperate to polar ice sheet configuration.

## CONCLUSIONS

A high-amplitude, laterally continuous package of subparallel reflectors has been identified on two high-resolution seismic sections, namely WEGA2601 and WEGA3501, in the George V land continental margin, Antarctica. Aiming to investigate the petrophysical properties associated with this anomalous package, we apply a seismic-to-well tie procedure at the IOPD site U1359 and the two high-resolution seismic sections where the anomalous package has been identified.

We apply a simple processing sequence to the raw seismic data and interpret the seismic sections identifying four main unconformities (WL-U6, WL-U7, WL-U7a and WL-U8) spanning from 13 to 4.5 Ma. The seismic-to-well tie is performed by comparing a synthetic trace with experimental stack traces in the nearby of the wells. Continuous velocity and density profiles from the sea floor to the bottom-hole are obtained by editing and integrating core-log measurements from the four wells characterizing the IOPD site U1359. The synthetic trace is modelled by convolving the reflectivity series, obtained from well-log data, with sea-floor reflections extracted from the seismic profiles.

We obtained a good matching with relatively high values of correlation coefficient (CC) and proportion of trace energy (PEP): CC = 0.72 and PEP = 0.51 for the line WEGA2601 and CC = 0.76 and PEP = 0.58 for the line WEGA3501. We improved the goodness-of-fit by stretching and squeezing the synthetics with a time variant cross-correlation procedure, reaching CC = 0.79 and PEP = 0.62 for the line WEGA2601 and CC = 0.81 and PEP = 0.66 for the line WEGA3501.

The successful tie between seismic and well-log data allowed us to recognize a direct link between the high amplitude reflectors that characterize the seismic unit between WL-U8 and WL-U7 with large density variations in the sedimentary sequence. In turn, the density variations are relatable to the alternation of diatom-rich and diamicton levels, deposited during phases of retreat (warm climate) or expansion (cold climate) of the marine ice sheet, respectively. This relationship between seismic amplitudes and sediment composition could be used to estimate distribution of diatom-rich versus diamicton layers on other sectors of the Antarctic margin. We suggest that the analysis of the characteristics and the distribution of similar seismic anomaly around Antarctica can give insight into the modality of past ice sheet dynamics. These results may find useful applications in

13652478, 0, Downloaded from https://onlinelibrary.wiley.com/doi/10.1111/1365-2478.13425 by Ogs Trieste Istituto Nazionale, Wiley Online Library on [13/11/2023]. See the Terms and Conditions (https://onlinelibrary.wiley.com/terms-and-conditions) on Wiley Online Library for rules of use; OA articles are governed by the applicable Creative Commons License

palaeoenvironmental analyses and possibly in predicting future scenarios related to the global warming.

Future works may focus on verifying the seismic-amplitude/sediment-composition relationship in other Integrated Ocean Drilling Program sites of the George V and nearby Wilkes lands and possibly along the continental margins of West Antarctica. Moreover, geotechnical analyses and a thorough well-log analysis of the alternation of diatom-rich diamicton sedimentary package may provide insight about the processes leading to the density, and consequently acoustic impedance, contrasts. Further studies may also deeply investigate the correlation between the frequency of climate cycles and the alternation in sediment-type as evidence by density change.

## ACKNOWLEDGEMENTS

Part of the well-log analysis and seismic-to-well tying has been performed with the Matlab packages Seislab3.01 (https://www.mathworks.com/matlabcentral/fileexchange/15674-seislab-3-01) developed by E. Rietsch, and CREWES (www.crewes.org) by T. Cui and G. F. Margrave. The authors also thank Aspen Technology Inc. for the academic license of the software Echos. The IHS supported this work with a Kingdom academic license released to OGS. This work is carried out in the frame of the PNRA19_00022 COLLAPSE project. The authors thank an anonymous reviewer whose comments and suggestions helped improve and clarify this manuscript.

Open Access Funding provided by Istituto Nazionale di Oceanografia e di Geofisica Sperimentale within the CRUI-CARE Agreement.

## DATA AVAILABILITY STATEMENT

The original wireline and core log data are available at the following sites: https://brg.ldeo.columbia.edu/data/iodp-usio/exp318/U1359D/, http://web.iodp.tamu.edu/OVERVIEW/?&exp=318&site=U1359. The WEGA and the RAE stack seismic lines are available from the Antarctic Data Library System (https://sdls.ogs.trieste.it) under the auspices of the Scientific Committee on Antarctic Research (SCAR) policy.

## ORCID

*Davide Gei* https://orcid.org/0000-0002-5755-6697

## REFERENCES

Anderson, P. & Newrick, R. (2008) Strange but true stories of synthetic seismograms. *CSEG Recorder*, 12, 51–56.

Bader, S., Wu, X. & Fomel, S. (2019) Missing log data interpolation and semiautomatic seismic well ties using data matching techniques. *Interpretation*, 7(2), T347–T361.

Bianco, E. (2014) Well-tie calculus. *The Leading Edge*, 33(6), 674–677.

Bianco, E. (2016) Tutorial: wavelet estimation for well ties. *The Leading Edge*, 35(6), 541–543.

Bisaso, I. (2011) Calibration of seismic and well data*: t*owards improved quantitative seismic reservoir characterisation of the Triassic to middle-Jurassic Gullfaks reservoir units of the Northern North Sea [Master's thesis]. Bergen: The University of Bergen.

Blackburn, T., Edwards, G.H., Tulaczyk, S., Scudder, M., Piccione, G., Hallet, B., et al. (2020) Ice retreat in Wilkes Basin of East Antarctica during a warm interglacial. *Nature*, 583(7817), 554–559. Available from: https://doi.org/10.1038/s41586-020-2484-5.

Bo, Y.Y., Lee, G.H., Kim, H.-J., Jou, H.-T., Yoo, D.G., Ryu, B.J., et al. (2013) Comparison of wavelet estimation methods. *Geosciences Journal*, 17(1), 55–63.

Brancolini, G. & Harris, P. (2000) *Post-cruise report AGSO survey 217: joint Italian/Australian Marine Geoscience Expedition aboard the R.V. Tangaroa to the George Vth Land Region of East Antarctica during, February–March, 2000*. AGSO Record 2000/38.

Cho, D. (2013) Cross-correlation based time warping of one-dimensional seismic signals. *CREWES Research Report*, 25, 1–6.

Cho, D. & Nordin, D. (2014) How much can I stretch and squeeze? *CSEG Recorder*, 39(10), 1–7.

Cui, T. (2015) Improving seismic-to-well ties [Master's thesis]. Calgary: University of Calgary.

Cui, T. & Margrave, G.F. (2015) Seismic-to-well ties by smooth dynamic time warping. *CREWES Research Report*, 27, 1–26.

Cook, C.P., Van De Flierdt, T., Williams, T., Hemming, S.R., Iwai, M., Kobayashi, M., et al. (2013) Dynamic behaviour of the East Antarctic Ice Sheet during Pliocene warmth. *Nature Geoscience*, 6(9), 765–769. Available from: https://doi.org/10.1038/ngeo1889

Dasgupta, T. & Mukherjee, S. (2020) Compaction of sediments and different compaction models. In: *Sediment compaction and applications in petroleum geoscience*. Cham: Springer, pp. 1–8.

Santis, L.D., Brancolini, G. & Donda, F. (2003) Seismo-stratigraphic analysis of the Wilkes Land continental margin (East Antarctica): influence of glacially driven processes on the Cenozoic deposition. *Deep Sea Research Part II: Topical Studies in Oceanography*, 50(8–9), 1563–1594.

Donda, F., Brancolini, G., Santis, L.D. & Trincardi, F. (2003) Seismic facies and sedimentary processes on the continental rise off Wilkes Land (East Antarctica): evidence of bottom current activity. *Deep Sea Research Part II: Topical Studies in Oceanography*, 50(8–9), 1509–1527.

Dorschel, B., Hehemann, L., Viquerat, S., Warnke, F., Dreutter, S., Tenberge, Y.S., et al. (2022) The International Bathymetric Chart of the Southern Ocean version 2. *Scientific Data*, 9, 275. https://doi.org/10.1038/s41597-022-01366-7.

Dutkiewicz, A., O'callaghan, S. & Müller, R.D. (2016) Controls on the distribution of deep-sea sediments. *Geochemistry, Geophysics, Geosystems*, 17(8), 3075–3098.

Escutia, C., Brinkhuis, H., Klaus, A. & IODP Expedition 318 Scientists (2011) Site U1359. *Proceedings of the Integrated Ocean Drilling Program*, 318, 1–120.

Ferraccioli, F., Armadillo, E., Jordan, T., Bozzo, E. & Corr, H. (2009) Aeromagnetic exploration over the East Antarctic Ice Sheet: a new view of the Wilkes Subglacial Basin. *Tectonophysics*, 478(1–2), 62–77. https://doi.org/10.1016/j.tecto.2009.03.013

Fomel, S. (2007) Local seismic attributes. *Geophysics*, 72(3), A29–A33. https://doi.org/10.1190/1.2437573

Gei, D. & Carcione, J.M. (2003) Acoustic properties of sediments saturated with gas hydrate, free gas and water. *Geophysical Prospecting*, 51, 141–158.

13652478, 0, Downloaded from https://onlinelibrary.wiley.com/doi/10.1111/1365-2478.13425 by Ogs Trieste Istituto Nazionale, Wiley Online Library on [13/11/2023]. See the Terms and Conditions (https://onlinelibrary.wiley.com/terms-and-conditions) on Wiley Online Library for rules of use; OA articles are governed by the applicable Creative Commons License

Gelpi, G.R., Pérez, D.O. & Velis, D.R. (2020) Automatic well tying and wavelet phase estimation with no waveform stretching or squeezing. *Geophysics*, 85(3), D83–D91.

Hale, D. (2009) A method for estimating apparent displacement vectors from time-lapse seismic images. *Geophysics*, 74(5), V99–V107.

Herrera, R.H. & Van Der Baan, M. (2014) A semiautomatic method to tie well logs to seismic data. *Geophysics*, 79(3), V47–V54.

Herrera, R.H., Fomel, S. & Van Der Baan, M. (2014) Automatic approaches for seismic to well tying. *Interpretation*, 2(2), SD9–SD17.

Iizuka, M., Seki, O., Wilson, D.J., Suganuma, Y., Horikawa, K., Van De Flierdt, T., et al. (2023) Multiple episodes of ice loss from the Wilkes Subglacial Basin during the Last Interglacial. *Nature Communications*, 14, 2129. https://doi.org/10.1038/s41467-023-37325-y.

Khim, B.-K., Song, B., Cho, H.G., Williams, T. & Escutia, C. (2017) Late Neogene sediment properties in the Wilkes Land continental rise (IODP exp. 318 hole U1359a), East Antarctica. *Geosciences Journal*, 21(1), 21–32.

Leys, C., Ley, C., Klein, O., Bernard, P. & Licata, L. (2013) Detecting outliers: do not use standard deviation around the mean, use absolute deviation around the median. *Journal of Experimental Social Psychology*, 49(4), 764–766.

Lloyd, H.J. & Margrave, G.F. (2013) The art of well tying with new Matlab tools. *CREWES Research Report*, 25, 1–12.

De Macedo, I.A.S., Da Silva, C.B. & De Figueiredo, J.J.S. & Omoboya, B. (2017) Comparison between deterministic and statistical wavelet estimation methods through predictive deconvolution: seismic to well tie example from the North Sea. *Journal of Applied Geophysics*, 136, 298–314.

Margrave, G.F. (2013) Why seismic-to-well ties are difficult. *CREWES Research Report*, 25, 1–26.

Orejola, N. & Passchier, S. (2014) Sedimentology of lower Pliocene to Upper Pleistocene diamictons from IODP Site U1358, Wilkes Land margin, and implications for East Antarctic Ice Sheet dynamics. *Antarctic Science*, 26(02), 183–192. Available from: https://doi.org/10.1017/S0954102013000527

Peterson, R.A., Fillippone, W.R. & Coker, F.B. (1955) The synthesis of seismograms from well log data. *Geophysics*, 20, 516–538.

Provenzano, G., Henstock, T.J., Bull, J.M. & Bayrakci, G. (2020) Attenuation of receiver ghosts in variable-depth streamer high-resolution seismic reflection data. *Marine Geophysical Research*, 41(2), 1–15.

Riedel, M., Collett, T., Malone, M. & the Expedition 311 Scientists (2006) Methods. In: *Proceedings of the Integrated Ocean Drilling Program*, vol. 311. Washington, DC: Integrated Ocean Drilling Program Management International.

Rietsch, E. (2021) SeisLab 3.01. MATLAB Central File Exchange. Available from: https://www.mathworks.com/matlabcentral/fileexchange/15674-seislab-3-01 [Accessed June 2021].

Rousseeuw, P.J. & Hubert, M. (2011) Robust statistics for outlier detection. *Wiley Interdisciplinary Reviews: Data Mining and Knowledge Discovery*, 1(1), 73–79.

Sams, M.S., Neep, J.P., Worthington, M.H. & King, M.S. (1997) The measurement of velocity dispersion and frequency-dependent intrinsic attenuation in sedimentary rocks. *Geophysics*, 62(5), 1456–1464.

Schwehr, K., Tauxe, L., Driscoll, N. & Lee, H. (2006) Detecting compaction disequilibrium with anisotropy of magnetic susceptibility. *Geochemistry Geophysics Geosystems*, 7, Q11002.

Simm, R. & Bacon, M. (2014) *Seismic amplitude: an interpreter's handbook*. Cambridge: Cambridge University Press.

Tauxe, L., Stickley, C.E., Sugisaki, S., Bijl, P.K., Bohaty, S.M., Brinkhuis, H., et al. (2012) Chronostratigraphic framework for the IODP expedition 318 cores from the Wilkes Land margin: constraints for paleoceanographic reconstruction. *Paleoceanography*, 27, PA2214.

Volpi, V., Camerlenghi, A., Hillenbrand, C.-D., Rebesco, M. & Ivaldi, R. (2003) Effects of biogenic silica on sediment compaction and slope stability on the Pacific margin of the Antarctic Peninsula. *Basin Research*, 15(3), 339–363.

White, R.E. & Simm, R. (2003) Tutorial: good practice in well ties. *First Break*, 21(10), 75–83.

Wilson, D.J., Bertram, R.A., Needham, E.F., Van De Flierdt, T., Welsh, K.J., et al. (2018) Ice loss from the East Antarctic Ice Sheet during late Pleistocene interglacials. *Nature*, 561(7723), 383–386. Available from: https://doi.org/10.1038/s41586-018-0501-8.

Wong, A.P.S. & Riser, S.C. (2011) Profiling float observations of the upper ocean under sea ice off the Wilkes Land coast of Antarctica. *Journal of Physical Oceanography*, 41(6), 1102–1115.

Yilmaz, Ö. (2001) *Seismic data processing*. Tulsa, OK: Society of Exploration Geophysicists.

Zhang, B., Yang, Y., Pan, Y., Wu, H. & Cao, D. (2020) Seismic well tie by aligning impedance log with inverted impedance from seismic data. *Interpretation*, 8(4), T917–T925.

**How to cite this article:** Gei, D., Brancolini, G., De Santis, L. & Geletti, R. (2023) Well-log integration and seismic-to-well tie off George V Land (Antarctica). *Geophysical Prospecting*, 1–20. https://doi.org/10.1111/1365-2478.13425

## APPENDIX A
## MEASURES OF GOODNESS-OF-FIT

The correlation coefficient (CC) is a common tool to measure the goodness-of-fit of two data series (Bianco, 2016; Herrera & van der Baan, 2014; White & Simm, 2003). It implicitly assumes an error-free synthetic seismogram (Bianco, 2016; White & Simm, 2003) and constitutes a measure of their linear dependence. Considering two time series $A = [a_1, a_2, a_3, \ldots, a_n]$ and $B = [b_1, b_2, b_3, \ldots, b_n]$, the CC is given by (Herrera & van der Baan, 2014)

$$\mathrm{CC} = \frac{\sum_{i=1}^{n} \left(a_i - \mu_A\right)\left(b_i - \mu_B\right)}{\sqrt{\sum_{i=1}^{n} \left(a_i - \mu_A\right)^2 \sum_{i=1}^{n} \left(b_i - \mu_B\right)^2}}, \qquad (A.1)$$

where $\mu$ indicates the mean. CC varies between $-1$ and 1: $\mathrm{CC} = 0$ means the data are uncorrelated, $\mathrm{CC} = 1$ indicates a prefect positive linear correlation and $\mathrm{CC} = -1$ indicates a prefect negative linear correlation, that is perfect correlation of signals with reverse polarity (Fomel, 2007).

13652478, 0, Downloaded from https://onlinelibrary.wiley.com/doi/10.1111/1365-2478.13425 by Ogs Trieste Istituto Nazionale, Wiley Online Library on [13/11/2023]. See the Terms and Conditions (https://onlinelibrary.wiley.com/terms-and-conditions) on Wiley Online Library for rules of use; OA articles are governed by the applicable Creative Commons License

The proportion of trace energy (PEP) is another measure of goodness-of-fit and is given by (e.g. Bisaso, 2011; Simm & Bacon, 2014)

$$\mathrm{PEP}\,(A, B) \;=\; 1 - \frac{\sum_i \left(a_i - b_i\right)^2}{\sum_i {a_i}^2}, \qquad \text{(A.2)}$$

where $A$ is the real seismic trace (observed), and $B$ is the synthetic trace (predicted). The term $(a_i - b_i)$ represents the residuals. PEP varies from negative values to 1. If $A = B$ the residuals are zero and PEP = 1; if the energy of the residuals is larger than the energy of the observed seismic trace, PEP is negative.

## APPENDIX B
## TIME VARIANT CROSS-CORRELATION

The time variant cross-correlation (TVCC) is a common method to improve the matching of two time series (e.g. Cho, 2013; Cui, 2015; Cui & Margrave, 2015; Hale, 2009). This technique is based on a running Gaussian window of the synthetic trace $\boldsymbol{B} = [b_1,\ b_2,\ b_3,\ \ldots, b_n]$, to be cross-correlated with the experimental data trace $A = [a_1,\ a_2,\ a_3,\ \ldots, a_n]$ with a user defined lag interval $t_{\mathrm{lag}}$. The lag $t_{\mathrm{shift}}$ resulting in the maximum TVCC coefficient is chosen to be the local time shift to be further applied to the centre of the Gaussian window (Cui & Margrave, 2015):

$$\max_t \left(B^{\sigma} \otimes A\right)(t), \qquad \text{(B.1)}$$

where $\sigma$ is the standard deviation (SD) of the Gaussian window, and $\otimes$ indicates the cross-correlation over time $t$. The input parameters to Equation (B.1) are the SD of the Gaussian window $\sigma$, the time interval between two subsequent windows $\tau$, which defines the centre of each Gaussian, and $t_{\mathrm{lag}}$. Small window width and large values of $t_{\mathrm{lag}}$ result in a better matching of the two time series but, they could produce abrupt changes of $t_{\mathrm{shift}}$, resulting in unphysical values of the modified velocity profile. To assure a smooth variation of $t_{\mathrm{shift}}$ with time, we slightly modified the original algorithm proposed by Cui and Margrave (2015) by applying to each Gaussian-windowed-portion of B the time shift of the previous window and using small values of $t_{\mathrm{lag}}$.

13652478, 0, Downloaded from https://onlinelibrary.wiley.com/doi/10.1111/1365-2478.13425 by Ogs Trieste Istituto Nazionale, Wiley Online Library on [13/11/2023]. See the Terms and Conditions (https://onlinelibrary.wiley.com/terms-and-conditions) on Wiley Online Library for rules of use; OA articles are governed by the applicable Creative Commons License